3D test simulations of the outer radiation belt electron dynamics including electron-chorus resonant interactions

Athina Varotsou [1], Daniel Boscher [2], Sebastien Bourdarie [2], Richard B. Horne [3], Nigel P. Meredith [3], Sarah A. Glauert [3], Reiner H. Friedel [1]

(1) Space Science and Applications, Los Alamos National Laboratory,
Los Alamos, NM, USA,
(2) Office National d'Etudes et Recherches Aérospatiales, Toulouse, France,
(3) British Antarctic Survey, Natural Environment Research Council, Cambridge, UK

athina@lanl.gov, daniel.boscher@oncert.fr, sebastien.bourdarie@onecert.fr, RH@bas.ac.uk,
nmer@bas.ac.uk, sagl@bas.ac.uk, friedel@lanl.gov

Abstract

We present results from our 3D simulations using the Salammbô electron radiation belt physical model. We have run steady state and dynamic storm test-case simulations to study the effect of electron-chorus resonant interactions on the radiation belt electron dynamics. When electron-chorus interactions are introduced in the code outside the plasmasphere, results show that a seed population with a kappa distribution and a characteristic energy of 2 keV is accelerated up to a few MeV in the outer radiation belt. MeV electron fluxes increase by an order of magnitude during high magnetic activity conditions especially near L^*~5 and for equatorial mirroring particles. We have also performed a parametric study of various important parameters to investigate how our results could be influenced by the uncertainty that characterizes their values. Results of this study show that if we consider higher values of the radial diffusion coefficients, different initial states and different boundary conditions, we always observe a peak in the L*-profile of the MeV electrons when electron-chorus interactions are included.

1. Introduction

Since the discovery of the radiation belts in 1958 [*Van Allen et al.*, 1958], a lot of progress has been made in understanding and describing the Earth's radiation environment. Scientific and operational satellite data combined with physical simulations have provided a great insight into the dynamics of the charged particle population and the physical processes involved.

One of the most important remaining questions is the definition of the physical processes responsible for the loss and acceleration of relativistic radiation belt electrons. During conditions of high geomagnetic activity these processes are enhanced causing the observed high variability of high energy electrons especially in the outer radiation belt. Relativistic electron fluxes will decrease if losses dominate, but if sources dominate, relativistic electron fluxes will increase, as is observed in approximately half of all moderate and intense geomagnetic storms [*Reeves at al.*, 2003]. The electron variation can be of several orders of magnitude on timescales from hours to days.

Several processes have been proposed to be responsible for the electron energization to MeV energies [e.g., *Friedel et al.*, 2002; *Horne*, 2002]. Radial diffusion was identified from the beginning as one of the most important [*Falthammar*, 1965, 1966]. Charged particles are transported inwards (towards the Earth) across magnetic field lines due to magnetic and electric field variations. Due to the conservation of the first adiabatic invariant (the particle's magnetic moment) particles moving towards regions of stronger magnetic field become more energetic. For equatorial particles the relationship between the energy of the particle and *L*- the distance (in Earth radii) of a magnetic field line from the center of the Earth at the equator [*McIlwain*, 1961]- is given by:

$$E_1(E_1 + 2E_0) * L_1^3 = E_2(E_2 + 2E_0) * L_2^3 \quad (1)$$

where E_1 and L_1 are the initial energy and distance (from the center of the Earth, in Earth radii) of the particle and E_2 and L_2 are the final energy and distance of the particle. E_0 is the rest energy of the electron which is equal to 0.511 MeV. In addition, enhanced ULF wave activity in the outer electron radiation belt has been associated with enhanced radial diffusion during high magnetic activity conditions [*O'Brien et al.*, 2001; *Elkington et al.*, 1999].

However, numerous recent studies have shown that radial diffusion alone cannot explain all the temporal and spatial flux variations observed [*Reeves et al.*, 1998; *Brautigam and Albert*, 2000; *Obara et al.*, 2000; *Miyoshi et al.*, 2003; *Horne et al.*, 2003b; *Green and Kivelson*, 2004; *Horne et al.*, 2005; *Chen et al.*, 2006; *Fox et al.*, 2006; *Iles et al.*, 2006; *Miyoshi et al.*, 2006; *Shprits et al.*, 2006c; *Chen et al.*, 2007]. *Brautigam and Albert* [2000] studied the October 9, 1991 storm using CRRES data. When they tried to reproduce the measured fluxes with a simple radial diffusion physical model their results underestimated relativistic electron fluxes around L = 4-4.5 and the flux increase during the recovery phase was not well represented by the model. From the data analysis they also observed outward radial diffusion from L = 4-5 during the recovery phase. The same storm was selected by *Horne et al.* [2003b] who studied the electron pitch angle distribution and found it to be energy dependent.

Miyoshi et al. [2006] used the 4D relativistic RAM electron model [*Jordanova et al.*, 1996, 2003; *Jordanova and Miyoshi*, 2005] to simulate the energetic electron dynamics during the October 2001 storm. Their results showed that radial diffusion, the only mechanism included in the model for relativistic energies (E>300 keV), was not sufficient to reproduce the observations. They concluded that an additional mechanism is needed to explain high energy electron enhancements during the storm's recovery phase.

Reeves et al. [1998], studied the global response of relativistic radiation belt electrons to the January 1997 magnetic cloud using data from LANL geosynchronous, GOES, GPS, POLAR, SAMPEX and HEO and showed that fluxes increased first near L = 4 and then at geosynchronous orbit, at L = 6.6.

Green and Kivelson [2004] in their study using POLAR data showed phase space density expressed data as a function of L^* and time for off-equatorial MeV electrons where a local peak appears near L^* = 4-5 during the recovery phase. Similar phase space density profiles were found by *Chen et al.* [2006, 2007] at the equator from combining POLAR, LANL geosynchronous and GPS data. Developing peaks in the electron phase space density were also found in the region $4 < L^* < 5.5$ during relativistic electron flux enhancements observed by the CRRES satellite [*Iles et al.*, 2006].

All the above results indicate that radial diffusion is not the only mechanism acting on radiation belt electrons in the outer belt and that a local source is acting which dominates other processes in the L = 4-5 region.

Many theoretical, observational and modeling studies have shown that the most probable mechanism acting locally as a high energy electron source is the resonant interaction of electrons with whistler-mode chorus waves leading to energy diffusion of lower energy particles to higher energy. The in situ wave-particle heating mechanism was theoretically discussed decades ago [*Kennel and Engelmann*, 1966; *Kennel*, 1969; *Lyons*, 1974] and agrees well with the scenario first proposed by *Thorne et al.* [1974] of important energy diffusion occurring outside the plasmasphere during active geomagnetic times when whistler-mode waves are present. More recently, *Horne and Thorne* [1998] studied different types of electromagnetic waves present in the magnetosphere to estimate the effect these waves could have on the trapped electron population. Whistler-mode waves in the low density environment outside the plasmasphere were found to be good candidates for electron acceleration to MeV energies from in situ energy diffusion of lower energy particles. Following theoretical studies also demonstrated that cyclotron and Landau resonances with whistler-mode chorus waves were the most probable mechanism to produce local acceleration to MeV energies [*Summers et al.*, 1998; *Horne et al.*, 2003a; *Glauert and Horne*, 2005].

Observational evidence for chorus-driven electron acceleration to relativistic energies has been mostly provided by CRRES data studies where both particle and plasma wave data were provided [*Meredith et al.*, 2002a,b, 2003a]. *Meredith et al.* [2003a] studied 26 geomagnetically disturbed periods and clearly showed the correlation between high levels of lower-band chorus activity and relativistic electron enhancements in the outer radiation belt. Similar studies are currently being performed using POLAR particle and wave data [*Kristine Sigsbee*, GEM 2007 poster and personal communication].

Apart from theoretical and observational evidence for chorus-driven electron acceleration to MeV energies, recent radiation belt 2D and 3D modeling efforts have focused on this topic also. *Varotsou et al.* [2005] presented the first results from 3D simulations with the Salammbô physical model [*Beutier and Boscher*, 1995; *Bourdarie et al.*, 1996] including both radial diffusion and energy diffusion due to electron-chorus resonant interactions. The simulations showed that when electron-chorus resonant interactions are included in the simulation, an initial seed population of electrons with characteristic plasmasheet energy of 5 keV can be locally accelerated to MeV energies in the outer belt near geosynchronous orbit.

In a two dimensional study by *Albert and Young* [2005] the diffusion equation was solved for energy and pitch angle diffusion due to chorus waves including the cross diffusion terms. The authors found that at L = 4.5 phase space density was strongly diffusing from 0.2 MeV up to a few MeV in less than a day.

Recently, *Li et al.* (2007) used the 2D UCLA radiation belt model, including energy and pitch-angle diffusion at a fixed L value and showed that the net effect of electron-chorus resonant interactions- including both dayside and night side parallel propagating chorus- is the local acceleration of relativistic electrons. The local increase of MeV fluxes during the recovery phase of a simulated storm persisted even after they introduced strong losses due to EMIC waves and plasmaspheric hiss.

In this paper we present a more detailed study that follows the first results presented by *Varotsou et al.* [2005]. We use the 3D Salammbô code to test the effect of each process (loss, acceleration, diffusion) on the flux and phase space density (PSD) profiles of relativistic electrons. The goal of our study is to investigate how different physical processes acting on the electrons influence the radiation belt dynamics. The study is performed for idealistic dynamic test-cases by using a physical model. The advantage of using a physical model is that we can 'turn on' or 'turn off' one of these processes to identify its effect on the radiation belt dynamics. We are not trying to reproduce satellite observations during a storm period at this point. More realistic simulations, using the actual *Kp* variation and a boundary condition from geosynchronous measurements and including high latitude chorus and EMIC waves, are being performed and will be presented in a following paper.

The outline of the paper is as follows. The Salammbô 3D model for radiation belt electrons is described in Section 2 and in Section 3 the diffusion coefficients for the electron-chorus interactions are presented together with the method we followed to introduce them into the code. The steady state and dynamic simulations are presented in Section 4, followed by a parametric study for several key parameters in Section 5. In Section 6 we discuss the limitations of the present study and our future goals, and in Section 7 we summarize the results and conclusions of our study.

2. The Salammbô 3D electron model

The development of the Salammbô 3D code for the Earth's radiation belts started in the 1990s at ONERA in Toulouse, France and continues until today [*Beutier and Boscher*, 1995; *Beutier et al.*, 1995; *Bourdarie et al.*, 1996; *Vacaresse et al.*, 1999; *Varotsou et al.*, 2005; *Maget et al.*, 2007]. There are two versions of the code, one for protons and one for electrons since the physical processes involved are different in each case. *Beutier and Boscher* [1995] first presented the electron physical model based on a Fokker-Planck diffusion equation solved in the (M,J,L^*) phase space, where M is the first adiabatic invariant, the particle's magnetic moment, J is the second adiabatic invariant related to the particle's bounce motion and L^* is the Roederer parameter [*Roederer*, 1970], related to the third adiabatic invariant Φ by $\Phi = 2\pi\alpha^2 B_0 / L^*$ (where α is the Earth's mean radius and B_0 is the equatorial magnetic field magnitude at the Earth's surface). Physical processes included were: radial diffusion, frictional processes by Coulomb interactions with plasmaspheric cold electrons, pitch angle diffusion by Coulomb interactions with atoms and molecules of the high atmosphere and pitch angle diffusion by wave-particle resonant interactions inside the plasmasphere. This version of the code was used by *Bourdarie et al.* [1996] in their effort to simulate the dynamics of radiation belt electrons during a magnetic storm.

The current version of the Salammbô 3D code solves the Fokker-Planck equation to estimate electron PSD in the (E,y,L^*) space, where E is the particle's kinetic energy, y is the sine of the particle's equatorial pitch angle, α_{eq}, and L^* is the Roederer parameter. The diffusion equation then translates to the following

$$\frac{\partial f}{\partial t} = L^{*2}\frac{\partial}{\partial L^*}\left(\frac{D_{LL}}{L^{*2}}\frac{\partial f}{\partial L^*}\right) + \frac{1}{yT(y)}\frac{\partial}{\partial y}\left(yT(y)D_{yy}\frac{\partial f}{\partial y}\right) + \frac{1}{a}\frac{\partial}{\partial E}\left(aD_{EE}\frac{\partial f}{\partial E}\right) - \frac{1}{a}\frac{\partial}{\partial E}\left(a\frac{dE}{dt}f\right) \qquad (2)$$

where the terms on the right hand side express radial diffusion, pitch angle diffusion (where $T(y)$ is an auxiliary function occurring in the bounce frequency expression), energy diffusion (where $a = (E+E_0)[E(E+2E_0)]^{1/2}$, E_0 the electron rest energy) and losses due to friction, respectively. Radial diffusion is assumed under constant first and second adiabatic invariants on one grid. Pitch angle diffusion occurs under constant energy and L^* and energy diffusion is considered under constant pitch-angle and L^* on a second grid. Interpolation methods are used between the two grids. We use logarithmic grids in energy and L^* and a uniform grid in pitch angle. No cross diffusion terms are included in the current version of the code. The introduction of cross diffusion terms is a difficult task which is under study and development [*Albert and Young*, 2005]. The magnetic field used in Salammbô is a dipolar, tilted and eccentric field.

The physical processes that drive radial, pitch angle and energy diffusion in the Salammbô code are described in Table 1 (see also diagram in Figure 1 of *Maget et al.*, 2007). The fourth and fifth columns indicate which calculation and which parameters were used for the definition of the diffusion coefficients. Note here that radial diffusion coefficients are different from the ones used by *Varotsou et al.* [2005].

Inside the plasmasphere, particles interact with hiss, VLF transmitters and lightning-generated whistlers. Outside the plasmasphere, particles interact with whistler-mode chorus waves. In this paper we mainly focus on the region outside the plasmapause where both radial diffusion and chorus waves occur (for more details on the plasmasphere and inner belt region refer to *Beutier and Boscher* [1995]).

In addition to these diffusive processes, particle energy loss by Coulomb interactions with cold plasmaspheric electrons and bound electrons of atoms and molecules of the high atmosphere are considered. This process is expressed by the frictional term in the diffusion equation (2). However, interactions with the high atmosphere don't have a significant effect on outer radiation belt electron dynamics, so we will not be analyzing this physical process in any detail (for more details see *Beutier and Boscher* [1995]).

In the code, the temporal evolution of PSD is determined by the temporal evolution of the coefficients introduced in the diffusion equation (2). Radial diffusion coefficients and pitch angle and energy diffusion coefficients due to chorus interactions outside the plasmasphere are expressed as a function of geomagnetic activity through the *Kp* index which is time dependent. Furthermore, the position of the plasmapause, which separates the regions where plasmaspheric waves and chorus operate, is also *Kp* dependent [*Carpenter and Park*, 1973]. The intensity of plasmaspheric waves is considered to be constant (not activity dependent) in Salammbô (see Discussion section). The expressions used for the diffusion coefficients together with the boundary conditions and our solving scheme of equation (2) will be described in the following Sections.

3. Electron – chorus resonant interactions

3.1 Diffusion coefficients from PADIE

Pitch angle, D_{yy}, and energy diffusion, D_{EE}, coefficients for cyclotron resonant electron - chorus interactions have been estimated from the PADIE code [*Glauert and Horne*, 2005]. The calculation is done using the quasi-linear assumption and is fully relativistic.

In the calculation, distributions of wave power and wave normal angles are assumed to be Gaussian [e.g. *Lyons*, 1974]. The wave distribution is considered to peak along the magnetic field direction with an angular spread of 30 degrees. Landau and ± 5 cyclotron harmonic resonances are included in the calculation and waves are assumed to be confined near the equator at magnetic latitudes of $-15^0 < \lambda_m < 15^0$. The conditions and parameters used for the calculation are the same as those used by *Varotsou et al.* [2005], presented here in Table 2. These values are based on wave observations from the Plasma Wave Experiment [*Anderson et al*., 1992] on board the CRRES spacecraft [*Glauert and Horne*, 2005].

Bounce averaged diffusion coefficients D_{yy} and D_{EE} are calculated by the PADIE code as a matrix with a constant wave amplitude of B_w = 100nT for electron plasma frequency to electron cyclotron frequency ratio (*fpe/fce*) values of 1.5, 2.5, 5.0, 7.5 and 10, electron energies of 0.01, 0.03, 0.1, 0.3, 1, and 3 MeV, and L values of 2.5, 3.5, 4.5, 5.5 and 6.5, with a resolution of less than 1 degree equatorial pitch angle. Diffusion coefficients are set to zero for energies $E < 0.01$ MeV and $E > 3$ MeV and for L values $L < 2.5$ and $L > 6.5$. For *fpe/fce* < 1.5 and *fpe/fce* > 10 diffusion coefficients are assumed constant and equal to their values for *fpe/fce* = 1.5 and *fpe/fce* = 10, respectively.

3.2 Introduction of D_{yy}, D_{EE} in Salammbô

The diffusion coefficients were related to magnetic activity by constructing a statistical wave model where equatorial values ($-15^0 < \lambda_m < 15^0$) of *f*pe/*f*ce and wave intensity B_{wave}^2 measured by CRRES were parameterized for $Kp < 2$, $2 \leq Kp \leq 4$ and $Kp \geq 4$ between L = 1 to 7, with a resolution of 0.1L and 1 hour in *MLT* [*Meredith et al.*, 2003b]. The coefficient values from the matrix given by PADIE were interpolated to energy, pitch angle and L values corresponding to the Salammbô grid and to *fpe/fce* values corresponding to the ones given from the statistical wave model (CRRES data).

For a given energy, L, pitch angle and Kp, the diffusion coefficients were calculated in each *MLT* bin according to *fpe/fce* and B_{wave}^2. Finally, for introduction in the Salammbô code, we calculated the coefficients' drift average by summing values over all MLT and dividing by the number of MLT bins. Since electron-chorus interactions are most efficient for low *fpe/fce* and high wave intensities [*Meredith et al.*, 2003b], they were only included in the model outside the plasmasphere.

An example of the bounce and drift averaged diffusion coefficients is presented in Figure 1 for $L^* = 4.8$. The first column shows the energy diffusion coefficients as a function of energy and equatorial pitch angle for the three different *Kp* categories and the second column shows the same dependence for the pitch angle diffusion coefficients. Some important conclusions can be drawn from Figure 1: a) both coefficients increase when geomagnetic activity (*Kp*) increases, b) for high energies both coefficients obtain higher values at higher pitch angles, thus acceleration will be more important near the equator and no high energy electron losses due to diffusion in the loss cone (low equatorial pitch angle values) by chorus waves will occur, and c) pitch angle diffusion for the low energy particles near the loss cone will be fast, thus these particles will experience important losses due to the interaction with chorus waves.

4. Test-case simulations

We solve the diffusion equation (2), using an explicit finite difference scheme, in the E, y ($=\sin\alpha_{eq}$), L^* space in a rectangular domain with 25 nodes in each direction (we chose the number of nodes for a fast execution since the time step of our calculations is limited by the Courant-Friedrichs-Lewy condition [*Courant et al.*, 1967]). The simulation domain in Salammbô extends for energies from 0.1 keV to 5 MeV, pitch angles from 2 degrees to 90 degrees (the lower limit for the equatorial pitch angle, under which electrons are lost in the upper atmosphere, is calculated in the model for each L^* shell- it doesn't take values of less than 2^0) and L^* shells from 1 to 8. Since electron-chorus interactions are introduced in the code for energies from 10 keV to 3 MeV and L^* values from outside the plasmapause to 6.5 and since our goal is to test if these interactions can lead to electron acceleration to MeV energies, the domain of interest in this study, on which we will focus, is for $E > 0.5$ MeV and $L^* > 3$.

The boundary conditions we impose for the solution of the diffusion equation are the following

$$f(E_{\min}) = f_{bound}(E_{\min}) \qquad f(E_{\max}) = 0$$

$$f(\alpha_{eq\,\min}) = 0 \qquad f(\alpha_{eq\,\max}) = \partial f / \partial \alpha = 0$$

$$f(L^*_{\min}) = 0 \qquad f(L^*_{\max}) = f_{bound}(E)$$

where f_{bound} is the outer boundary condition (only a function of electron energy) we impose at $L^* = 8$, which constitutes the source of electrons in the simulation. In our current study this condition is constant with time (a time varying boundary is currently being studied and will be presented in a future paper). With the above boundary conditions we consider that: a) the lowest energy PSD- at the outer boundary- stays constant and there is an absence of multi-MeV energies, b) the loss cone is empty and the pitch angle particle distribution at the equator is flat, and c) losses dominate at $L^* = 1$ and the source at $L^* = 8$ is constant and given by the f_{bound} boundary condition.

The boundary condition at $L^* = 8$ is defined to be a kappa distribution [*Christon et al.*, 1991] given by the formula

$$f_{bound} = A\left[1 + \frac{E}{kE_0}\right]^{-k-1} \qquad (3)$$

where we take $A = 10^{35}$ $MeV^{-3}s^{-3}$, defined by examining a long period of LANL geosynchronous measurements, $E_0 = 2$ keV (plasmasheet characteristic energy) , defined by average LANL geosynchronous MPA (Magnetospheric Plasma Analyzer) data [*Joseph Borovsky* private communication 2007] and $k = 5$, based on *Christon et al.* [1988, 1991]. Note here that *Varotsou et al.* [2005] used a kappa distribution with a characteristic energy of 5 keV, considering a higher energy spectrum at the source.

Finally, to help the reader follow the work and results presented in the following Sections we summarize in Table 3 the physical processes involved in radiation belt dynamics outside the plasmasphere in Salammbô, together with the expressions of the coefficients introduced in the diffusion equation (2) and the simulation domain where each process is included. The plasmapause position is defined by the empirical expression $Lpp = 5.6 - 0.46Kp'$ [*Carpenter and Park*, 1973], where Kp' is the highest value of the Kp index during the last 24 hours of the simulation.

4.1. Steady state

First we present the results obtained for a steady state of the radiation belts. There is no dynamics and no time dependence involved here. This permits us to detect the effect electron-chorus interactions have on the radiation belt electrons when we include them in our simulation scheme. In addition, the initial state for the dynamic simulation is defined from the output of this steady state simulation.

In the steady-state simulation, the diffusion equation (2) is solved for $\partial f/\partial t = 0$. The steady state is defined for a certain geomagnetic activity level, i.e., for a given Kp value. When we fix Kp to a constant value, radial diffusion coefficients depend only on L^*, while pitch angle and energy diffusion coefficients depend on energy, pitch angle and L^*, and the plasmapause is fixed to a certain L^* shell.

Radiation belts are considered to initially be empty everywhere except at the outer boundary (L^* = 8) where the source is defined by equation (3). After many iterations, the system reaches a steady state and the calculated phase space densities represent the state of the radiation belts after a long period of steady conditions.

We run the code for Kp = 1.3 to use the output as an initial state of calm conditions for our dynamic simulation. To investigate the effect of electron-chorus resonant interactions on the electron distribution we performed one simulation including this process and one without it. The results are presented in Figures 2, 3 and 5.

4.1.1. PSD variation as a function of L shell

In Figure 2, phase space densities are presented as a function of L^* shell and iteration number for a constant magnetic moment value of M = 2100 MeV/G and for equatorial mirroring particles (α_{eq} = 90 degrees). The plasmapause position is marked with a white line.

In these type of plots, energy increases as we move inwards to lower L^* shells. For M = 2100 MeV/G, we are studying ~1 MeV electrons at L^* ~ 6 and ~2 MeV electrons at L^* ~ 4.5. We choose to represent results in a (M, α_{eq}) = constant space instead of a (M, J) = constant space (where J is the second adiabatic invariant) because we want to be able to distinguish between different processes affecting the electron distribution. In addition, α_{eq} = constant is not that different from J = constant.

Figure 2(a) shows results when electron-chorus interactions are included in the simulation together with radial diffusion. First, particles are transported inwards (in the initially empty radiation belts) from the outer boundary by radial diffusion and then they are accelerated by chorus waves resulting to the formation of a peak in the PSD distribution at L^* ~ 5-6. Then, phase space density at surrounding L^* shells (lower than 5 and higher than 6) increases due to radial diffusion diffusing particles away from the peak. As a result, phase space density increases inside the plasmasphere and outside L^* = 6.5, regions where electron-chorus interactions are not considered in the simulation.

In contrast, in Figure 2(b), where results with only radial diffusion included in the simulation are shown, there is no peak forming in the PSD distribution in L^* shell. Particles are only diffused inwards forming a flat PSD distribution. The maximum difference in the PSD values between the two steady states is observed at L^* = 5.5 and is equal to two orders of magnitude. These kinds of increases have been observed at geosynchronous and GPS orbits [*Chen et al.*, 2007].

4.1.2. PSD variation as a function of equatorial pitch angle

In Figure 3, results from the two simulations (with and without chorus waves) are presented for comparison as a function of equatorial pitch angle for L^* = 5.2 and for E = 1.7 MeV. We choose to present results with respect to energy, equatorial pitch angle and L^* values to confirm that introduction of electron-chorus interactions in a 3D particle simulation leads to energy diffusion, i.e., acceleration of electrons to MeV energies.

When electron-chorus resonant interactions are introduced in the simulation we observe an increase in the PSD level. This increase is greater for equatorial pitch angles of 50 degrees and higher. Flat top pitch angle distributions like this are a signature of chorus wave acceleration and have been observed by the CRRES satellite (*Horne et al.*, 2003b).

The profile of the red curve (when chorus waves are included in the simulation) can be explained if we look at the profile of the energy and pitch angle diffusion coefficients as a function of equatorial pitch angle. Both coefficients are plotted in Figure 4 for the same parameters as in Figure 3. Energy diffusion coefficients obtain maximum and almost steady values for equatorial pitch angles between 60 and 90 degrees. For α_{eq} < 60 degrees, D_{EE} decreases very fast with decreasing pitch angle, becoming one order of magnitude smaller every ~10 degrees. Pitch angle diffusion coefficients are higher in the region of 50-70 degrees. Their role is to diffuse equatorial particles to lower pitch angle values. Thus, PSD values increase for all equatorial pitch angles (red curve in Figure 3).

In general we conclude that the effect of introducing chorus waves in our simulations is most important for equatorial particles, down to a value of α_{eq}~50 degrees. This is related to our initial hypothesis that chorus waves are confined near the equator (see Discussion section).

4.1.3. PSD variation as a function of energy

Finally, in Figure 5, results are presented as a function of energy for L^* = 5.2 and for equatorial particles (α_{eq}=90 degrees). As in the previous figures, results from the simulation with electron-chorus interactions (red curve) and without (blue curve) are compared. When chorus waves are included, energy diffusion- by which lower energy electrons are accelerated to higher energies- becomes very important. Higher energy phase space densities increase significantly, while lower energy (less than 30 keV) phase space densities decrease. As an example, 600 keV and 1.7 MeV electron phase space densities increase by more than 2 orders of magnitude while ~ 20 keV electron PSD becomes 2 times smaller.

In reality we don't see low energies decreasing while higher ones increase. The decrease of the low energy phase space densities is an artifact of our simulations since we are considering a constant outer source and convection is not included in the simulation. Observations show that times of enhanced chorus activity coincide with times of enhanced injections and substorm activity [*Meredith et al.*, 2001, 2002a, 2003a]. Thus, the low energy source increases during these times.

4.2 Dynamic simulation

During high geomagnetic activity conditions, variations in the trapped electron distribution can be important and in many cases very fast. Modeling these variations requires a good understanding of the physical processes involved in radiation belt- and magnetospheric- dynamics.

Here, the goal is to expand the study on the combined effect of radial diffusion and electron-chorus resonant interactions presented by *Varotsou et al.* [2005]. We have simulated a simple test-case where *Kp* varies step-wise from a low initial value to a higher one and then back to the initial one. The *Kp* profile for this simulation is shown in Figure 6. We chose *Kp* to be initially equal to 1.3 to simulate calm conditions. This initial state is the steady state calculated in the previous section. Then, *Kp* becomes equal to 4 for one day and finally it returns to its initial low value. Next, we will focus on the evolution of the electron distributions from time *T1* (initial state) to time *T2* (state after 1 day of *Kp* = 4) shown in Figure 6.

4.2.1. PSD as a function of L shell

When *Kp* increases, both radial diffusion and electron-chorus interactions are enhanced. To identify which process is responsible for the dynamics observed we perform three simulations: one where both radial diffusion and chorus interactions are included, one where we 'turn off' radial diffusion and one where we 'turn off' electron-chorus interactions. The initial state used is the same for all simulations. The results from the three simulations at time *T2* are plotted in Figure 7. In this figure, phase space densities are plotted versus L^* shell for equatorial particles with magnetic moment equal to 2100 MeV/G. Also marked (vertical dashed lines) is the plasmapause position for $Kp = 1.3$ and $Kp = 4$.

When we 'turn off' radial diffusion, interactions with chorus waves are the only process acting on radiation belt electrons outside the plasmasphere. As a result, at time *T2* phase space densities increase significantly creating a very pronounced peak at $L^* = 5.7$. This increase is confined in the region where chorus waves are defined in our simulation ($Lpp < L^* < 6.5$) and is maximal in the $L^* = 5$-6 region (increase of more than 2 orders of magnitude).

When we 'turn off' electron-chorus interactions, radial diffusion is the only process acting on electrons outside the plasmasphere. In this case, at time *T2* phase space densities decrease at higher L^* shells ($L^* > 4.5$) and increase at lower L^* shells. This is the result of particles diffusing away from the peak that already exists in the initial state. During high activity conditions, enhanced outward radial diffusion from the peak- at $L^* \sim 5$- towards higher L^* results in the decrease of PSD since particles are lost at the boundary (which stays constant in our simulation). Inward radial diffusion is weaker, but we can see a small increase in PSD at $L^* < 4.5$.

Finally, when both processes are included in the simulation, the localized effect of chorus waves is diffused by radial diffusion to all L^* shells. The peak value decreases while values around the peak increase. This increase is more important at higher L^* shells where radial diffusion is stronger, resulting at an important increase of PSD in the region where chorus waves are not considered in the simulation ($L^* > 6.5$) [*Varotsou et al.,* 2005]. However, the most important increase in the PSD-L^* distribution- more than an order of magnitude- is observed near L^* = 5-6 (E = 1-2 MeV).

4.2.2. PSD as a function of equatorial pitch angle and energy

In Figure 8, results from all three simulations ('turning off' chorus, 'turning off' radial diffusion and including both processes) are plotted versus equatorial pitch angle at L^* = 5.2 and for E = 1.7 MeV particles. At this L^* we position ourselves at the peak of the PSD distribution as shown in Figure 7 (red line).

Results agree well with those presented in Figure 7. Radial diffusion, when acting alone, diffuses particles away from the peak in the initial PSD-L^* distribution decreasing PSD at the peak location. This process is equally strong at all equatorial pitch angles- since the D_{LL} coefficients do not depend on α_{eq}- but its effect depends also on $\partial f/\partial L$ at each α_{eq} value.

When chorus interactions is the only process acting, PSD increases by a factor of ~ 100 for $\alpha_{eq} > 40$ degrees. Energy and pitch angle diffusion are much weaker at low equatorial pitch angles for MeV electrons (see Figure 1 and 4).

When both processes are taken into account, radial diffusion weakens the effect of chorus waves for $\alpha_{eq} > 30$ degrees by diffusing particles away from the peak created by chorus interactions. However it is obvious that chorus interactions dominate over radial diffusion at $\alpha_{eq} > 30$ degrees and the overall result is a net increase of electron PSD (more than an order of magnitude) for these pitch angle values outside the plasmasphere.

In Figure 9, PSD is plotted versus energy (from 0.5 to 5 MeV) and equatorial pitch angle for $L^* = 5.2$ at times *T1* and *T2*. Phase space densities have greatly increased at time *T2* at the MeV energy range for $\alpha_{eq} > 30$ degrees in agreement with the results presented in Figure 8. However at lower pitch angle values no increase is observed for the MeV particles. To understand this behavior better we plot in Figure 10 for $Kp = 4$, as a function of energy, (a) pitch angle diffusion coefficients D_{yy} for $\alpha_{eq} = 85$ degrees (solid line) and $\alpha_{eq} = 30$ degrees (dash dot line) and (b) energy diffusion coefficients D_{EE} for $\alpha_{eq} = 90$ degrees (solid line) and $\alpha_{eq} = 30$ degrees (dash dot line).

For α_{eq} = 70-90 degrees we do not expect pitch angle diffusion to play an important role, since, as it is noted in Section 4.1, the initial pitch angle distribution at *T1* is flat near these values. In this region, energy diffusion is principally responsible for the dynamics observed especially at higher energies as can be seen in Figure 10(b) for $\alpha_{eq} = 90$ degrees.

At $\alpha_{eq} = 30$ degrees the coefficient's values are very different from those at 90 degrees. Figure 10(b) shows that energy diffusion coefficients for high energy electrons become 10^3 times weaker (even more in some cases). As a result, the increase of high energy phase space densities in Figure 9 is much weaker at $\alpha_{eq} \sim 30$ degrees than at higher ones.

4.2.3. Fluxes

Since PSD is not a physical quantity that is measured by satellites, we show here our results for the dynamic test-case simulation including both radial diffusion and electron-chorus interactions as fluxes. In Figure 11, omnidirectional fluxes at the equator are shown in an L^*-time space for 1.6 MeV. The plasmapause location is shown with a green line and the *Kp* variation with time is shown on the top of the figure.

Once again we clearly observe the electron acceleration due to chorus interactions: MeV fluxes increase in the heart of the radiation belts when activity increases. After 1 day of $Kp = 4$ fluxes become 24 times higher at $L^* = 5.7$ and 15 times higher at $L = 6.6$. When *Kp* recovers to its initial low value, MeV fluxes keep increasing at $L^* > 6$ due to radial diffusion. After the plasmapause relaxes to its initial position MeV fluxes inside the plasmasphere decrease slowly.

5. Parametric study

In Sections 3 and 4 we presented the results of simulations including chorus interactions in the Salammbô 3D code. The results showed clearly that a low energy seed population can be locally accelerated by chorus waves to MeV energies in the heart of the radiation belts near $L^* = 5$. However, many of the parameters used in the simulations are quite uncertain, thus it is important to perform a parametric study where the sensitivity of the results to the parameter's values can be quantified. Here we examine how results change if we consider different values for three of the important parameters: 1) radial diffusion coefficients, 2) initial state condition and 3) source condition at $L^* = 8$.

5.1. Radial diffusion coefficients

The accurate definition of radial diffusion coefficients constitutes one of the most important projects in radiation belt physics. Although many efforts have been made to calculate them empirically [*Lanzerotti et al.*, 1970; *Lanzerotti and Morgan*, 1973; *Holzworth and Mozer*, 1979; *Brautigam and Albert*, 2000; *Li*, 2004] and theoretically [*Falthammar*, 1965, 1966; *Schulz and Lanzerotti*, 1974; *Brizard and Chan,* 2001; *Perry et al.*, 2005], there is still a lot of uncertainty concerning their dependence in *L*, energy, pitch angle and magnetic activity.

As noted in previous sections, the result of the simulation performed using both radial diffusion and chorus interactions depends on the relative intensity of the two processes. If radial diffusion coefficients had lower values than the ones used here [*Brautigam and Albert*, 2000] then the effect of chorus waves on the electron distribution would be even more important. Here we examine how results change if we consider higher radial diffusion coefficient values.

To investigate the influence of the radial diffusion coefficient's uncertainty on our results we perform two simulations, increasing D_{LL} by a factor of three and six, respectively. The results of both simulations for the steady case are plotted in Figure 12(a), together with the previous result- with the nominal *Brautigam and Albert* [2000] coefficient values. The steady case simulation is for Kp = 1.3 and for M = 2100 MeV/G equatorial particles. The number of iterations used is the same for all simulations.

Figure 12(a) shows that there is an important difference between the results of the three simulations. When higher values are used for the radial diffusion coefficients, PSD profiles become much more flat, or completely flat for the case where D_{LL} is increased by a factor of 6. Radial diffusion erases almost completely the effect of chorus wave interactions by diffusing particles away from the peak that tends to be created.

In Figure 12(b), results from the dynamic simulations are plotted versus L^* for 2100 MeV/G equatorial electrons. The dynamic simulation performed here is the same dynamic test-case simulation as the one presented in Section 4.2: starting from an initial low activity state (steady state for Kp = 1.3) we calculate the state of the electron radiation belts after 1 day of high magnetic activity (1 day of Kp = 4). For the simulations presented here, the common initial state used is a flat PSD distribution which corresponds to the steady state calculated by using six times higher D_{LL} values.

Results after one day of Kp = 4 (time *T2*) are presented for the three different D_{LL} values. The first thing that we notice is that even when an initial flat distribution is used, irrespective of the size of D_{LL} used, the effect of chorus waves is easily distinguishable: electrons are locally accelerated to MeV energies and a peak forms near L^* = 5.

The differences between the three curves at time *T2* are at the location of the peak and at the level of PSD. When higher D_{LL} values are used, the peak is less pronounced, moves inwards in L^* and is characterized by lower PSD values. In these cases radial diffusion is more effective in diffusing particles away from the peak that chorus interactions tend to create. In addition, strong outward radial diffusion is more effective at high L^* values, thus the peak of the electron distribution is now observed at lower L^* shells.

5.2. Initial state condition

We compare the dynamics resulting after 1 day of Kp = 4 for two different initial state conditions as shown in Figure 13. State 1 has a flat L^*-profile and State 2 has a 'peaked'

L^*-profile with higher PSD values. From the comparison between dynamic state 1 (Dyn 1) and dynamic state 2 (Dyn 2) we conclude that phase space densities increase much faster in the case where the flat, lower initial state is used, reaching peak values similar to the ones for the case where the higher peaked initial state is used. The two initial states are different by a factor of ~115 at the peak location ($L^* = 5.2$), however the two dynamic states are different by only a factor of ~ 6.

The reason for this difference is the fact that radial diffusion will initially be much weaker in the simulation using State 1, since $\partial f/\partial L = 0$ for all L^* values greater than $L^* = 5$. In this case, radial diffusion will become stronger only when a peak has started forming due to chorus waves. However, in the simulation where State 2 is used, radial diffusion will be strong from the beginning since significant peak in the PSD L^*-profile exists initially.

5.3. Boundary condition

The outer boundary condition is an important parameter in the simulation. We chose to use a characteristic energy of 2 keV for the plasma sheet which is the average value measured at geosynchronous orbit [*Joseph Borovsky*, private communication 2007]. However, at geosynchronous altitude- near $L^* = 6.6$- it is also measured that this temperature increases when magnetic activity increases, taking values of up to 5 keV [*Joseph Borovsky*, private communication 2007].

In this Section we investigate the sensitivity of the simulation results to the boundary condition. For this we consider two additional boundary conditions: one expressed by a similar kappa distribution with characteristic energy of 5 keV (similar to the one used in

Varotsou et al., [2005]) and one obtained empirically from CRRES measurements (used in radial diffusion studies [*Shprits and Thorne, 2004; Shprits et al.*, 2005; *Shprits et al.,* 2006b]). The latter is defined by an exponential fit of the average flux measured by CRRES at L^* = 7 and it is given by the expression

$$J = 8222.6 * 10^3 \exp\left(-E/0.141\right) \qquad (4)$$

Where J is the differential flux (in $cm^{-2}sr^{-1}MeV^{-1}s^{-1}$) and E is the kinetic energy of the particle (in MeV). Differential fluxes at L^* = 7 are converted into PSD and then PSD values are relaxed adiabatically to L^* = 8 by assuming that the particle's magnetic moment is conserved. This assumption is based on the fact that only radial diffusion occurs in the L^* = 7-8 region in the Salammbô code.

Both conditions are assumed to be constant with time like the one that was used in simulations presented before (kappa distribution with E_0 = 2 keV). By keeping the boundary condition constant we are able to clearly identify the effect of chorus waves on the electron dynamics. The effect of a time dependent boundary condition is currently being studied and will be presented in a future paper (see Discussion section).

The spectra of the three source conditions at the outer boundary are shown in Figure 14. If a higher characteristic energy kappa distribution is considered, PSD of higher energies increases and thus the $\partial f/\partial E$ values become smaller. As a result, we expect energy diffusion to be less important for this case. The second boundary condition from CRRES defines lower PSD values at low energies (E < 100 keV) and higher PSD values for E = 100 keV – 1 MeV, compared to those defined by the kappa distribution with E_0 = 2 keV.

We must note here that we extrapolated the CRRES spectrum for $E < 153$ keV since the MEA detector only measured fluxes for energies higher than 153 keV. This may not be the most realistic approach but provides us with another test case to study the effect of the boundary condition on the MeV electron dynamics. To avoid any confusion we will call this condition the modified CRRES boundary condition.

We have performed the same dynamic simulation as described in Section 4.2 for both new boundary conditions. Results are presented in Figures 15 (a), (b) and (c) for 2100 MeV/G equatorial electrons for all three boundaries at times *T1* and *T2* of the dynamic test-case simulation. First thing we observe is that all boundary conditions produce a local peak in the PSD L^*-profile at time *T2* at similar locations- near $L^* = 5$. The most important difference can be noted for the case when the modified CRRES condition is used. For this case, the increase of PSD is less important than in the other two cases, even though a higher energy source is defined. This is due to the fact that the energy spectrum defined by this condition determines lower and flatter phase space densities at energies lower than 100 keV. As a result, the source is smaller and the energy diffusion due to chorus wave interactions weaker.

However, a higher energy spectrum at the source does not affect the amount of energization. Differences observed between Figure 15(a) and (b) at time *T2* are due to the difference in the initial states at time *T1* (see section 5.2).

6. Discussion

The conclusions of our study are clearly shown and supported throughout this paper, however, our simulations have important limitations. One of the first and most important assumptions that we made was that chorus waves are confined near the equator. Adding the effect of chorus waves at higher latitudes will affect the acceleration rate of electrons but also their losses since losses are mostly determined by the value of $D\alpha\alpha$ near the edge of the loss cone [*Shprits et al.,* 2006a]. Various observations have shown that chorus waves are present at higher latitudes [*Tsurutani and Smith*, 1977; *Meredith et al.*, 2003b]. *Meredith et al*. [2003b] used CRRES data to show that dayside chorus waves are mostly confined to higher latitudes ($\lambda > 15$ degrees) in contrast to night side chorus which are mostly confined near the equator. When *Li et al.* [2007] introduced dayside high latitude chorus (parallel propagating only), together with night side equatorial chorus, into their 2D simulations MeV losses at high latitudes became important, however the net result was still electron acceleration.

Another limitation of our simulation is imposed by the fact that energy and pitch angle diffusion coefficients due to chorus interactions are limited to a certain L^* space. Recent observations have shown that chorus wave emissions can be detected at L^* shells up to $L^* = 10$ [*Santolík et al.*, 2005], however in our simulations they are confined at $L^* < 6.5$. This prevents us from estimating the relative power of chorus interactions and radial diffusion outside $L^* = 6.2$, which is the last grid point inside $L^* = 6.5$ in Salammbô.

In addition, diffusion coefficients due to chorus interactions are defined for three *Kp* categories: $Kp < 2$, $2 \leq Kp < 4$ and $Kp \geq 4$. The first two categories are small but the third one is very broad (from 4 to 9) and it is the one that interests us the most. This broad categorization is due to limited statistics for $Kp \geq 4$. However, radial diffusion coefficients continuously increase with increasing geomagnetic activity. The *Kp* categorization for the chorus wave effect makes it hard to directly compare with the radial diffusion effect, especially if we want to simulate higher than *Kp* = 4 storms.

The precision of the *Kp* parameterization of wave intensity and f_{pe}/f_{ce} using the CRRES data can also be questioned. In the first half of the mission, when the satellite was on the dayside (at dawn), activity was weak, however, on the second half of the mission, when the satellite was on the night side (at dusk), activity was high. For this second part, chorus activity for low *Kp* values may be overestimated. In addition, as it can be seen in Figure 1 of *Meredith et al.* [2003b], there exists an important data gap above $L^* = 5$ near $MLT = 10$.

These limitations are also pointed out by *Maget et al.* [2007] when they run the Salammbô 3D code using data assimilation techniques and found that when they included chorus wave interactions in the scheme, fluxes were overestimated in the region inside $L = 4$ as compared to the CRRES data.

More wave observations are needed for the better definition and understanding of the region where chorus waves are interacting with electrons, their relation to magnetic activity and their propagation characteristics. Many current observational studies focus on the determination of the source and spatial distribution of chorus emissions using data from POLAR [*Kristine Sigsbee*, private communication 2007], CLUSTER and DOUBLE STAR [*Santolík et al.*, 2004, 2005]. More data will be available in the future with the upcoming Radiation Belt Storm Probes mission.

We also think that the dependence of radial diffusion coefficients on energy and pitch angle need to be further investigated. In the work presented here we chose to use the diffusion coefficients estimated by *Brautigam and Albert* [2000] since these are the values generally used by the radiation belt community. These coefficients depend on *L*-shell and magnetic activity (*Kp* parameter). *Varotsou et al.* [2005] used radial diffusion coefficients based on calculations by *Schulz* [1991] that are energy, pitch angle and L dependent. A magnetic activity dependence was added based on a calculation using data from the CRRES satellite. Magnetic radial diffusion coefficients by *Schulz* [1991] become ~ 7 times weaker at α_{eq} = 20 degrees compared to their equatorial values. Thus, results presented in this paper are similar to the ones presented by *Varotsou et al.* [2005] for equatorial mirroring particles but different results are obtained for low α_{eq} values (not shown in *Varotsou et al*. [2005]). In the case where coefficients by *Schulz* [1991] are used, we don't observe the decrease at α_{eq} < 30 degrees, as seen in Figure 8, in Section 4.2.2. Recently, *Perry et al*. [2005] calculated radial diffusion coefficients by incorporating spectral characteristics of Pc5 waves into 3D simulations using the guiding center approximation. They found that when a data-based, frequency and *L*-dependent model is used for the wave power, an important decrease in radial diffusion coefficients occurs as the mirror latitude increases from 0 degrees (equator) to 20 degrees.

Finally, we must note the absence of the cross diffusion coefficient $D_{\alpha E}$ in equation (2). The effect of this coefficient on the final result is still a subject of discussion. The high values of the coefficient as calculated by the PADIE code [*Glauert and Horne*, 2005]- sometimes even higher than the energy diffusion coefficient- suggest that its effect will be important. A recent study by *Albert and Young* [2005] showed that when the cross term is introduced in the diffusion equation results are qualitatively similar, but for small α_{eq} energy diffusion is overestimated if the cross diffusion is neglected. The cross diffusion term is not included in any current 3D radiation belt code.

Our current priority is to validate the new code by simulating a real storm. A more realistic study of the radiation belt dynamics during geomagnetic storm conditions, where the *Kp* and boundary variation are taken from real data, is currently being performed and will be presented in a future paper.

Another important development of our code is the introduction of higher latitude day side chorus. As discussed above, these waves are expected to introduce MeV electron losses into the loss cone.

In addition, other wave types are currently being studied for introduction in the Salammbô code. Recent studies have shown that enhanced EMIC waves in plasmaspheric plumes formed during the storm's main phase (e.g., *Erlandson and Ukhorskiy*, 2001) can cause strong MeV electron losses from pitch angle diffusion in the loss cone (*Thorne and Kennel*, 1971; *Albert*, 2003; *Summers and Thorne*, 2003). Plasmaspheric hiss is currently included in the code but it is independent of geomagnetic activity. Our current goal is to introduce activity dependent hiss, since studies have shown that hiss is enhanced during active conditions [*Meredith et al.,* 2004].

Finally, we want to underline the importance of comparing results obtained from different codes. We hope that in the future we will be able to work with other teams in comparing simulation results. However this has to be done with much caution since the assumptions considered in each model are different.

7. Conclusions

We have run steady state and dynamic test-case simulations to study the effect of electron-chorus resonant interactions on the radiation belt electron dynamics. We used the Salammbô 3D physical model which includes radial diffusion and particle-wave interactions inside and outside of the plasmasphere. Simulations were performed where both electron-chorus interactions and radial diffusion were included in the code but we also run simulations with only one of the two processes included. In that way we were able to identify the role of each of these two key physical processes on the radiation belt dynamics. The main results of our study are the following:

1. The introduction of chorus interactions in the Salammbô code leads to the local acceleration of electrons to MeV energies.
2. Acceleration during dynamic test-case simulations of moderate activity conditions ($Kp = 4$) is stronger at $L^* \sim 5$ and for equatorial pitch angles near 90 degrees.
3. The net effect of a geomagnetic storm- the peak value and location- is defined by the relative power between chorus interactions and radial diffusion.
4. Simulation results are not sensitive to the high energy distribution of the source, however they are sensitive to the low energy distribution ($E < 100$ keV).

Our results support the following scenario: during active geomagnetic periods low energy electrons are transported inwards from an outer source location by enhanced convection and radial diffusion, a fraction of them are energized locally to MeV energies by chorus interactions. At the same time radial diffusion acts diffusing particles inwards and outwards from the peak that tends to form in the PSD distribution.

References

Abel, B. and R. M. Thorne (1998a), Electron scattering loss in Earth's inner magnetosphere 1. Dominant physical processes, *J. Geophys. Res., 103,* 2385.

Abel, B. and R. M. Thorne (1998b), Electron scattering loss in Earth's inner magnetosphere 2. Sensitivity to model parameters, *J. Geophys. Res., 103,* 2397.

Albert, J. M., and S. L. Young (2005), Multidimensional quasi-linear diffusion of radiation belt electrons, *Geophys. Res. Lett.*, *32*, L14110, doi:10.1029/2005GL023191.

Anderson, R. R., D. A. Gurnett, and D. L. Odem (1992), CRRES plasma wave experiment, *J. Spacecr. Rockets*, *29*,(4), 570-573.

Beutier, T., and D. Boscher (1995), A three-dimensional analysis of the electron radiation belt by the Salammbô code, *J. Geophys. Res., 100*, 14,853.

Beutier, T., D. Boscher, and Martin France (1995), SALAMMBO: A three-dimensional simulation of the proton radiation belt, *J. Geophys. Res., 100*, 17,181.

Bourdarie, S., D. Boscher, T. Beutier, J.-A. Sauvaud, and M. Blanc (1996), Magnetic storm modeling in the Earth's electron belt by the Salammbô code, *J. Geophys. Res., 101*, 27,171-27,176.

Brautigam, D. H., and J. M. Albert (2000), Radial diffusion analysis of outer radiation belt electrons during the October 9, 1990, magnetic storm, *J. Geophys. Res.*, *105*, 291.

Brizard, A. J., and Chan, A. A. (2001), Relativistic bounce-averaged quasi-linear diffusion equation for low frequency electromagnetic fluctuations, *Phys. Of Plasmas*, Vol. 8, 11, doi:10.1063/1.1408623.

Carpenter, D. L., and C. G. Park (1973), On what ionosphere workers should know about the plasmapause-plasmasphere, *Rev. Geophys., 11*, 133.

Chen, Y., R. H. W. Friedel, and G. D. Reeves (2006), Phase space density distributions of energetic electrons in the outer radiation belt during two Geospase Environment Modeling Inner Magnetosphere/Storms selected storms, J. *Geophys. Res., 111*, A11S04, doi:10.1029/2006JA011703.

Chen, Y., G. D. Reeves and R. H. W. Friedel (2007), The energization of relativistic electrons in the outer Van Allen radiation belt, *Nature Physics*, doi:10.1038/nphys655.

Christon, S. P., D. G. Mitchell, D. J. Williams, L. A. Frank, C. Y. Huang, and T. E. Eastman (1988), Energy spectra of plasma sheet ions and electrons from ~50eV/e to ~1 MeV during plasma temperature transitions, *J. Geophys. Res., 93*, 2562.

Christon, S. P., D. J. Williams, D. G. Mitchell, C. Y. Huang, and L. A. Frank (1991), Spectral characteristics of plasma sheet ion and electron populations during disturbed geomagnetic conditions, *J. Geophys. Res., 96*, 1.

Courant, R., K. Friedrichs, and H. Lewy (1967), On the Partial Difference Equations of Mathematical Physics, *IBM J.* 11, 215-234.

Elkington, S. R., M. K. Hudson, and A. A. Chan (1999), Acceleration of relativistic electrons vis drift-resonant interaction with toroidal-mode Pc-5 ULF oscillations, *Geophys. Res. Lett.*, *26*, 3273-3276.

Fälthammar, C.G. (1965), Effects of time-dependent electric fields on geomagnetically trapped radiation, *J. Geophys. Res., 70*, 2503.

Fälthammar, C.G. (1966), On the transport of trapped particles in the outer magnetosphere, *J. Geophys. Res., 71*, 1487.

Fox, N. J., B. H. Mauk, and J. B. Blake (2006), Role of non-adiabatic processes in the creation of the outer radiation belts, *Geophys. Res. Lett., 33*, L18108, doi:10.1029/2006GL026598.

Friedel, R. H., G. D. Reeves, and T. Obara (2002), Relativistic electron dynamics in the inner magnetosphere- A review, *J. Atmos. Sol. Terr. Phys.*, *64*, 265.

Glauert, S. A. and R. B. Horne (2005), Calculation of pitch angle and energy diffusion coefficients with the PADIE code, *J. Geophys. Res., 110*, doi:10.1029/2004JA010851.

Green, J. C., and M. G. Kivelson (2004), Relativistic electrons in the outer radiation belt: Differentiating between acceleration mechanisms, *J. Geophys. Res., 109*, A03213, doi:10.1029/2003JA010153.

Hedin, A. E. (1979), Tables of thermospheric temperature, density and composition derived from satellite and ground based measurements, *Rep. N79-18515, vol.1-3*, NASA Goddard Space Flight Center, Greenbelt, Md.

Holzworth, R. H., and F. S. Mozer (1979), Direct evaluation of the radial diffusion coefficient near L = 6 due to electric field fluctuations, *J. Geophys. Res.*, *84*, 2559.

Horne, R. B. (2002), The contribution of wave particle interactions to electron loss and acceleration in the Earth's radiation belts during geomagnetic storms, in *USRI Review of Radio Science 1999-2002*, edited by W. R. Stone, pp. 801-828, chap. 33, John Wiley, Hoboken, N. J.

Horne, R. B., and R. M. Thorne (1998), Potential waves for relativistic electron scattering and stochastic acceleration during magnetic storms, *Geophys. Res. Lett.*, *25,* 3011.

Horne, R. B., S. A. Glauert, and R. M. Thorne (2003a), Resonant diffusion of radiation belt electrons by whistler-mode chorus, *Geophys. Res. Lett., 30*, 1493, doi:10.1029/2003GL016963.

Horne, R. B., N. P. Meredith, R. M. Thorne, D. Heynderickx, R. H. A. Iles, and R. R. Anderson (2003b), Evolution of energetic electron pitch angle distributions during storm time electron acceleration to megaelectronvolt energies, *J. Geophys. Res., 108*, 1016, doi:10.1029/2001JA009165.

Horne, R. B., R. M. Thorne, Y. Y. Shprits, N. P. Meredith, S. A. Glauert, A. J. Smith, S. G. Kanekal, D. N. Baker, M. J. Engebretson, J. L. Posch, M. Spasojevic, U. S. Inan, J. S. Pickett, and P. M. E. Decreau (2005), Wave acceleration of electrons in the Van Allen radiation belts, *Nature*, Vol 437, doi:10.1038/nature03939.

Jordanova, V. K., L. M. Kistler, J. U. Kozyra, G. V. Kazanov, and A. F. Nagy (1996), Collisional losses of ring current ions, *J. Geophys. Res.*, *101*, 111.

Jordanova, V. K., A. Boonsiriseth, R. M. Thorne, and Y. Dotan (2003), Ring current asymmetry from global simulations using a high-resolution electric field model, *J. Geophys. Res.*, *108*(A12), 1443, doi:10.1029/2003JA009993.

Jordanova, V. K., and Y. S. Miyoshi (2005), Relativistic model of ring current and radiation belt ions and electrons: Initial results, *Geophys. Res. Lett.*, *32*, L14104, doi:10.1029/2005GL023020.

Iles, R. H. A., N. P. Meredith, A. N. Fazakerley, and R. B. Horne (2006), Phase space density analysis of the outer radiation belt energetic electron dynamics, *J. Geophys. Res.*, *111*, A03204, doi:10.1029/2005JA011206.

Kennel, C. F. (1969), Consequences of a magnetospheric plasma, *Rev. Geophys., 7*, 379.

Kennel, C. F., and F. Engelmann (1966), Velocity space diffusion from weak plasma turbulence in a magnetic field, *Phys. Fluids, 9*, 2377.

Lanzerotti,L. J., and C. G. Morgan (1973), ULF geomagnetic power near L = 4-2: Temporal variation of the radial diffusion coefficient for relativistic electrons, *J. Geophys. Res.*, *78*,4600.

Lanzerotti, L. J., C. G. MacLennan, and M. Schulz (1970), Radial diffusion of outer-zone electrons: An empirical approach to third-invariant violation, *J. Geophys. Res.*, *75*, 5351.

Li, X. (2004), Variations of 0.7-6.0 MeV electrons at geosynchronous orbit as a function of solar wind, *Sp. Weather*, Vol. 2, No. 3, S0300610.1029/2003SW000017.

Li, W., Y. Y. Shprits, and R. M. Thorne (2007), Dynamic evolution of energetic outer zone electrons due to wave-particle interactions during storms, *J. Geophys. Res.*, accepted.

Lyons, L. R. (1974), General relations for resonant particle diffusion in pitch angle and energy, *J. Plasma Phys., 12*, 45-49.

Maget, V., S. Bourdarie, D. Boscher, and R. H. W. Friedel (2007), Data assimilation of LANL satellite data into the Salammbô electron code over a complete solar cycle by direst insertion, *Sp. Weather*, 2007SW000322.

McIlwain, C.E. (1961), Coordinates for mapping the distribution of magnetically trapped particles, *J. Geophys. Res., 66*, 3681-3691.

Meredith, N. P., R. B. Horne, and R. R. Anderson (2001), Substorm dependence of chorus amplitudes: Implications for the acceleration of electrons tp relativistic energies, *J. Geophys. Res.*, *106*, 13,165.

Meredith, N. P., R. B. Horne, R. H. A. Iles, R. M. Thorne, D. Heyndrickx, and R. R. Anderson (2002a), Outer zone relativistic electron acceleration associated with substorm-enhanced whistler-mode chorus, *J. Geophys. Res., 107*, 1144.

Meredith, N. P., R. B. Horne, D. Summers, R. M. Thorne, R. H. A. Iles, D. Heynderickx, and R. R. Anderson (2002b), Evidence for acceleration of outer zone electrons to relativistic energies by whistler mode chorus, *Ann. Geophys., 20*, 967.

Meredith, N. P., M. Cain, R. B. Horne, R. M. Thorne, D. Summers, and R. R. Anderson (2003a), Evidence for chorus-driven electron acceleration to relativistic energies from a survey of geomagnetically-disturbed periods, *J. Geophys. Res., 108*(A6), 1248, doi:10.1029/2002JA009764.

Meredith, N. P., R. B. Horne, R. M. Thorne, and R. R. Anderson (2003b), Favored regions for chorus-driven electron acceleration to relativistic energies in the Earth's outer radiation belt, *Geophys. Res. Lett., 30*, 1871, doi:10.1029/2003GL017698.

Meredith, N. P., R. B. Horne, R. M. Thorne, D. Summers, and R. R. Anderson (2004), Substorm dependence of plasmaspheric hiss, *J. Geophys. Res., 109,* A06209, doi:10.1029/2004JA010387.

Miyoshi, Y., A. Morioka, T. Obara, H. Misawa, T. Nagai, and Y. Kasahara (2003), Rebuilding process of the outer radiation belt during the 3 November 1993 magnetic storm: NOAA and Exos-D observations, *J.Geophys. Res., 108*(A1), 1004, doi:10.1029/2001JA007542.

Miyoshi, Y. S., V. K. Jordanova, A. Morioka, M. F. Thomsen, G. D. Reeves, D. S. Evans, and J. C. Green (2006), Observations and modeling of energetic electron dynamics during the October 2001 storm, *J. Geophys. Res.*, *111*, A11S02, doi:10.1029/2005JA011351.

Obara, T., T. Nagatsuma, M. Den, Y. Miyoshi, and A. Morioka (2000), Main-phase creation of ‘seed’ electrons in the outer radiation belt, *Earth Planets Space, 52*, 41-47.

O’Brien, T. P., R. L. McPherron, D. Sornette, G. D. Reeves, R. H. Friedel, and H. J. Singer (2001), Which magnetic storms produce relativistic electrons at geosynchronous orbit?, *J. Geophys. Res.*, *106*(8), 15,533, doi:10.1029/2001JA000052.

Perry, K. L., M. K. Hudson, and S. R. Elkington (2005), Incorporating spectral characteristics of Pc5 waves into three-dimensional radiation belt modeling and the diffusion of relativistic electrons, *J. Geophys. Res.*, *110*, A03215.

Reeves, G. D., D. N. Baker, R. D. Belian, J. B. Blake, T. E. Cayton, J. F. Fennell, R. H. W. Friedel, M. M. Meier, R. S. Selesnick and H. E. Spence (1998), The global response of relativistic radiation belt electrons to the January 1997 magnetic cloud, *Geophys. Res. Lett., 25*(17), 3265.

Reeves, G. D., K. L. McAdams, R. H. Friedel, and T. P. O’Brien (2003), Acceleration and loss of relativistic electrons during geomagnetic storms, *Geophys. Res. Lett.*, *30*(10), 1529, doi:10.1029/2002GL016513.

Roederer, J. G., Dynamics of Geomagnetically Trapped Radiation, Springer-Verlag, New York, 1970.

Santolík, O., D. A. Gurnett, and J. S. Pickett (2004), Multipoint investigation of the source region of storm-time chorus, *Ann. Geophys.*, 22, 2555-2563.

Santolík, O., E. Macúšová, K. H. Yearby, N. Cornilleau-Wenhrlin, and H. StC. K. Alleyne (2005), Radial variation of whistler-mode chorus: first results from the

STAFF/DWP instrument on board the Double Star TC-1 spacecraft, *Ann. Geophys.*, 23, 2937-2942.

Schulz, M. (1991), The magnetosphere, geomagnetically trapped radiation, in *Geomagnetism*, vol. 4, edited by J. A. Jacobs, pp. 202-256, Elsevier, New York.

Schulz, M., and L. Lanzerotti (1974), Particle Diffusion in the Radiation Belts, Springer, New York.

Shprits, Y. Y., and R. M. Thorne (2004), Time dependent radial diffusion modeling of relativistic electrons with realistic loss rates, *Geophys. Res. Lett., 31*, L08805, doi:10.1029/2004GL019591.

Shprits Y. Y., and R. M. Thorne (2006a), Controlling effect of the pitch angle scattering rates near the edge of the loss cone on the electron lifetime, *J. Geophys. Res.*, *111*, A12206, doi:10.1029/2006JA011758.

Shprits Y. Y., R. M. Thorne, R. Friedel, G. D. Reeves, J. Fennell, D. N. Baker, S. G. Kanekal (2006b), Outward radial diffusion driven by losses at the magnetopause, *J. Geophys. Res.*, *111*, A11214, doi:10.1029/2006JA011657.

Shprits Y. Y., R. M. Thorne, R. B. Horne, S. A. Glauert, M Cartwright, C. T. Russel, D. N. Baker, S. G. Kanekal (2006c), Acceleration mechanism responsible for the formation of the new radiation belt during the 2003 Halloween solar storm, *Geophys. Res. Lett.*, *33*, L05104, doi:10.1029/2005GL024256.

Shprits, Y. Y., R. M. Thorne, G. D. Reeves, and R. H. Friedel (2005), Radial diffusion modeling with empirical lifetimes: comparison with CRRES observations, *Ann. Geophys.*, 23, 1467-1471.

Summers, D., R. M. Thorne, and F. Xiao (1998), Relativistic theory of wave-particle resonant diffusion with application to electron acceleration in the magnetosphere, *J. Geophys. Res., 103*, 20,487.

Thorne, R. M., E. J. Smith, K. J. Fiske, and S. R. Church (1974), Intensity variation of ELF hiss and chorus during isolated substorms, *Geophys. Res. Lett., 1*, 193-196.

Tsurutani, B. T. and E. J. Smith (1977), Two types of magnetospheric chorus and their substorm dependencies, *J. Geophys. Res.*, *82*, 5112.

Vacaresse, A, D. Boscher, S. Bourdarie, M. Blanc, and J.-A. Sauvaud (1999), Modeling the high-energy proton belt, *J. Geophys. Res., 104*, 28,601.

Van Allen, J.A., G.H. Ludwig, E.C. Ray, and C.E. McIlwain (1958), Observations of high intensity radiations by satellites 1958 alpha and gamma, *Jet. Propul.*, *28*, 588.

Varotsou, A., D. Boscher, S. Bourdarie, R. B. Horne, S. A. Glauert, and N. P. Meredith (2005), Simulation of the outer radiation belt electrons near geosynchronous orbit including both radial diffusion and resonant interaction with Whistler-mode chorus waves, *Geophys. Res. Lett., 32*, L19106, doi:10.1029/2005GL023282.

Figure captions

Figure 1. Energy and pitch angle diffusion coefficients due to chorus interactions, as a function of energy and equatorial pitch angle for three *Kp* categories at $L^* = 4.8$.

Figure 2. Steady state phase space density calculation (in $MeV^{-3}s^{-3}$) for 2100 MeV/G equatorial particles and $Kp = 1.3$, for two simulations: (a) including chorus wave interactions and (b) including only radial diffusion.

Figure 3. Steady state phase space density (in $MeV^{-3}s^{-3}$) as a function of equatorial pitch angle for 1.7 MeV electrons at $L^* = 5.2$ and for $Kp = 1.3$, for two simulations: (a) including chorus wave interactions (red line) and (b) including only radial diffusion (blue line).

Figure 4. Energy and pitch angle diffusion coefficients (in s^{-1}) as a function of equatorial pitch angle, for $L^* = 5.2$, $E = 1.7$ MeV and $Kp = 1.3$.

Figure 5. Steady state phase space density (in $MeV^{-3}s^{-3}$) as a function of energy for equatorial particles at $L^* = 5.2$ and for $Kp = 1.3$, for two simulations: including chorus wave interactions (red line) and including only radial diffusion (blue line).

Figure 6. *Kp* profile for the dynamic test-case simulation.

Figure 7. Phase space densities (in $MeV^{-3}s^{-3}$) for 2100 MeV/G equatorial electrons as a function of L^* from the three simulations at time *T2*: including only chorus wave interactions (orange line), including only radial diffusion (blue line) and including both processes (red line), starting from the same initial state (black line). Dashed lines show the position of the plasmapause for $Kp = 1.3$ and $Kp = 4$.

Figure 8. Phase space densities (in $MeV^{-3}s^{-3}$) for 1.7 MeV electrons at $L^* = 5.2$ as a function of equatorial pitch angle from the three simulations at time *T2*.

Figure 9. 2D plots of phase space densities at L^* = 5.2 as a function of energy (shown from 0.5 to 5 MeV on a log scale) and equatorial pitch angle at a) time T1 and b) time T2.

Figure 10. Diffusion coefficients as a function of energy for Kp = 4 and L^* = 5.2: (a) pitch angle diffusion coefficients at α_{eq} = 85 degrees (solid line) and 30 degrees (dash dot line) and (b) energy diffusion coefficients at α_{eq} = 90 degrees (solid line) and 30 degrees (dash dot line).

Figure 11. Omnidirectional equatorial flux variation during the test-case simulation for 1.6 MeV electrons. The plasmapause position is marked with a green line.

Figure 12. Phase space densities (in $MeV^{-3}s^{-3}$) for 2100 MeV/G equatorial particles as a function of L^* for (a) the three steady state simulations and (b) at time *T2* for the three dynamic simulations starting from the same initial state at *T1* (black line).

Figure 13. Phase space densities (in $MeV^{-3}s^{-3}$) for 2100 MeV/G equatorial particles as a function of L^* at times *T1* and *T2* from two dynamic simulations: one starting from State 1 and one starting from State 2.

Figure 14. Spectrum of the three distributions used as a source at the outer boundary (L^* = 8): the kappa distribution with E_0 = 2 keV (red line), the kappa distribution with E_0 = 5 keV (blue line) and the modified CRRES distribution (black line).

Figure 15. Phase space densities (in $MeV^{-3}s^{-3}$) for 2100 MeV/G equatorial particles as a function of L^* at times *T1* and *T2* using the three boundary conditions: (a) a kappa distribution with E_0 = 2 keV, (b) the kappa distribution with E_0 = 5 keV and (c) the modified CRRES distribution.

Table1. Diffusive processes in Salammbô

Physical Process (1)	**Effect (2)**	**Coefficients (3)**	**Calculation (4)**	**Parameters (5)**
Field fluctuations	Radial Diffusion	$D_{LL}^{(m)}$	*Brautigam and Albert* (2000)	*Brautigam and Albert* (2000)
Particle-wave interactions *inside* plasmasphere	Pitch angle diffusion	D_{yy}	*Abel and Thorne* (1998a)	Described in: *Abel and Thorne* (1998b)
Coulomb collisions with high atmosphere	Pitch angle diffusion	D_{yy}	*Schulz and Lanzerotti (1974)*	Atmospheric densities from MSIS 86 model[a] [*Hedin*, 1979]
Particle-wave interactions *outside* plasmasphere	Energy diffusion and pitch angle diffusion	D_{EE}, D_{yy}	PADIE code: *Glauert and Horne* (2005)	CRRES data: Glauert and Horne (2005) and Meredith et al. (2003b)

[a] Plus a hydrostatic model above 800 km for each species

Table 1. Physical processes included in Salammbô, their effect on radiation belt electrons, the coefficients that express their effect in the diffusion equation and the references for the calculation and the parameters used to estimate the coefficients.

Table 2. Chorus wave characteristics

Parameter	**Assumed distribution**	**Characteristic values**
Wave power	Gaussian distribution	Peak: $0.35f_{ce}$ Bandwidth: 0.15*fce* Lower cut-off: 0.125*fce* Upper cut-off: 0.575*fce*
Wave normal angle	Gaussian distribution $X = \tan(\psi)$	Peak: $X_m = 0$ Angular spread: $X_w = \tan(30^0)$ $X_{min} = 0$ $X_{max} = 1$

Table 2. The wave characteristics used for the calculation of the pitch angle and energy diffusion coefficients due to chorus wave interactions.

Table 3. Diffusive processes outside the plasmapause

Diffusive process	Coefficients	Domain of application
Radial Diffusion	$D_{LL} = 10^{(0.506Kp-9.325)}\, L^{10}$	applied everywhere in our simulation domain
Pitch-angle and energy diffusion due to chorus waves	PADIE coefficient matrix for $D_{\alpha\alpha}$ and D_{EE} for 3 *Kp* categories	Plasmapause $< L \leq 6.5$ 10 keV $\leq E \leq$ 3MeV all α_{eq} values

Table 3. The two diffusive physical processes included in Salammbô outside the plasmapause, their expressions and the simulation domain of application.

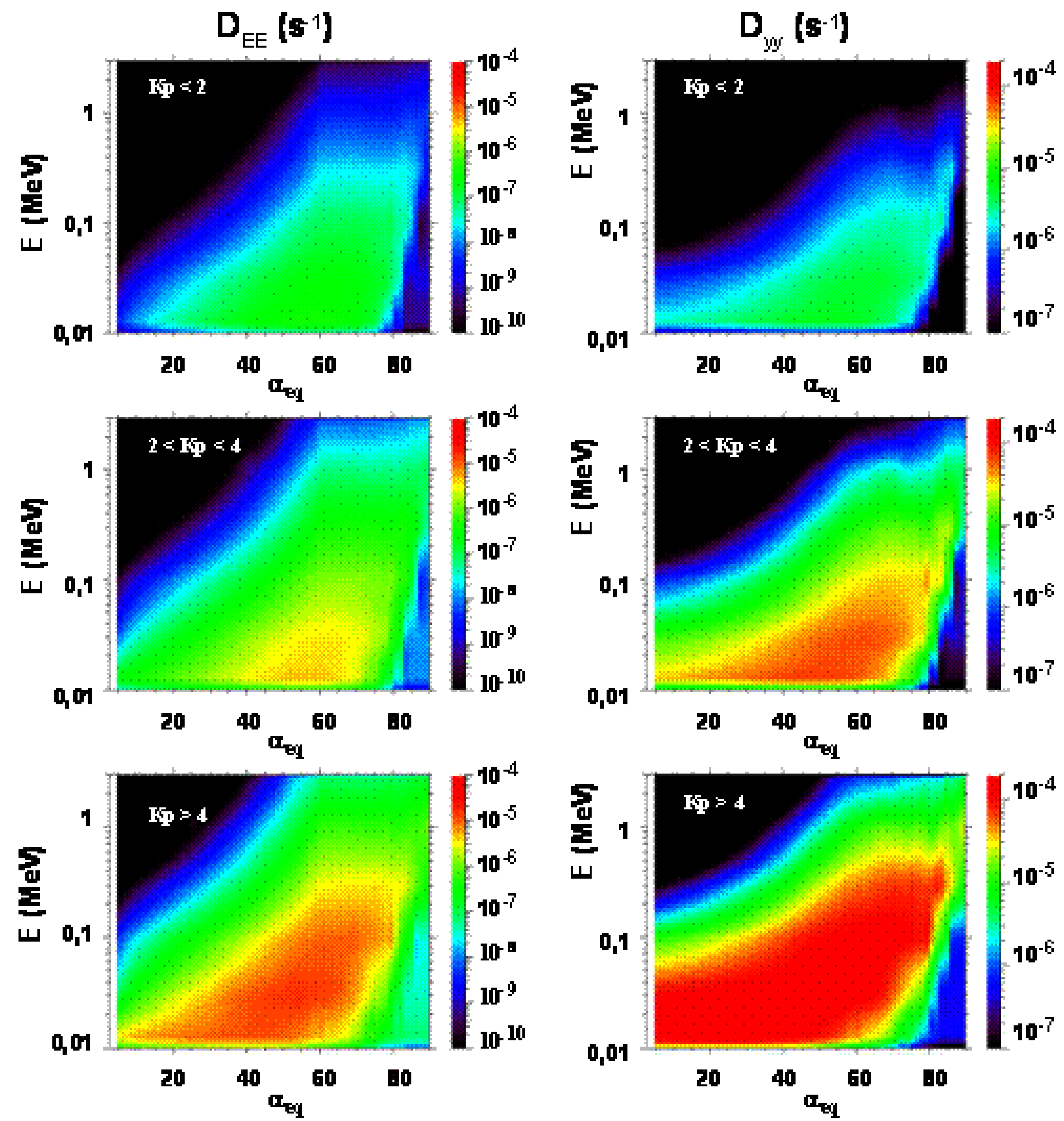

D_{EE} (s^{-1})
D_{yy} (s^{-1})
Kp < 2
2 < Kp < 4
Kp > 4
E (MeV)
α_{eq}
0,01
0,1
1
20
40
60
80
10^{-4}
10^{-5}
10^{-6}
10^{-7}
10^{-8}
10^{-9}
10^{-10}

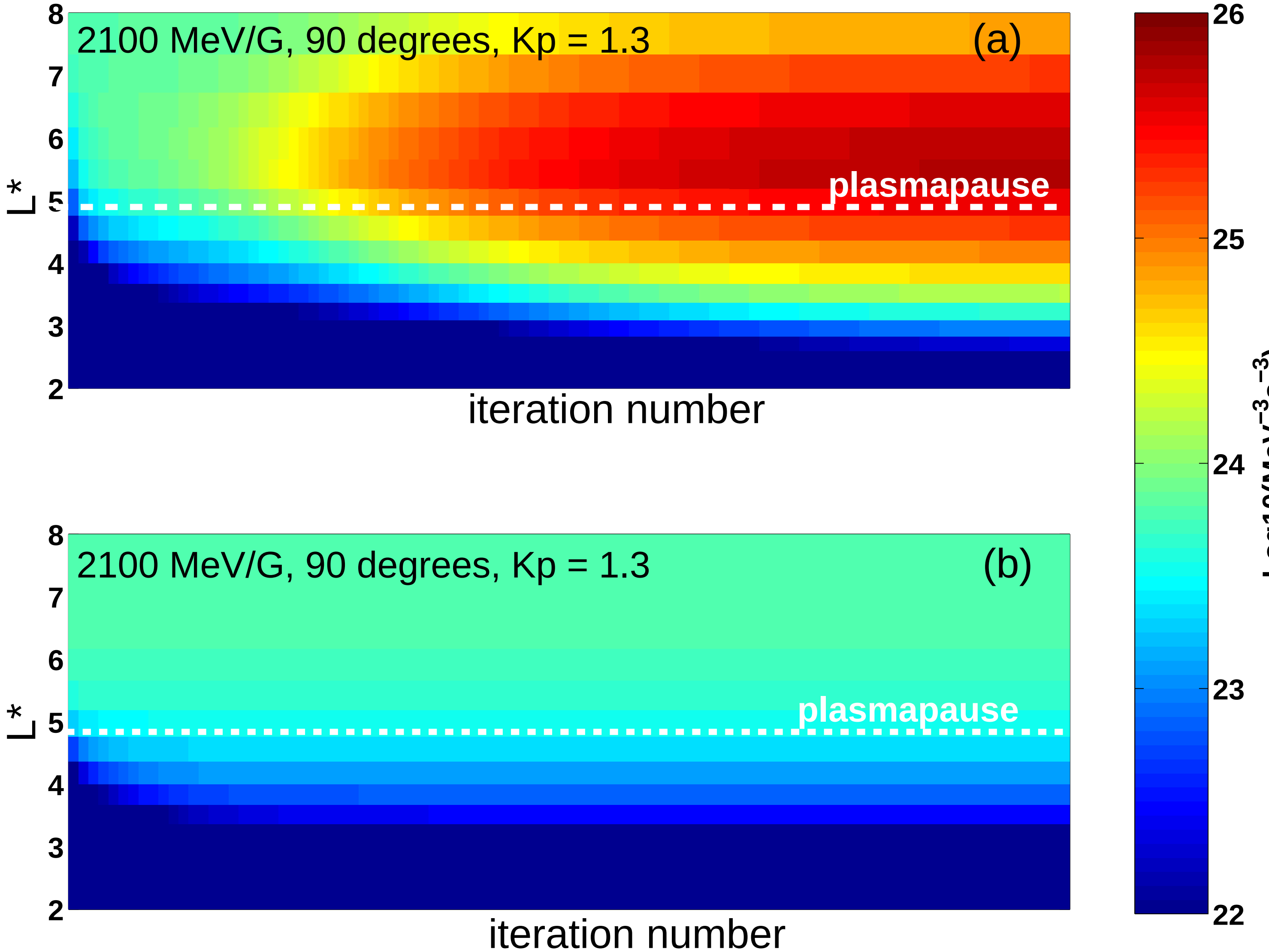

Figure 2. Steady state phase space density calculation (in MeV−3 s−3) for 2100 MeV/G equatorial particles and Kp = 1.3, for two simulations: (a) including chorus wave interactions and (b) including only radial diffusion.

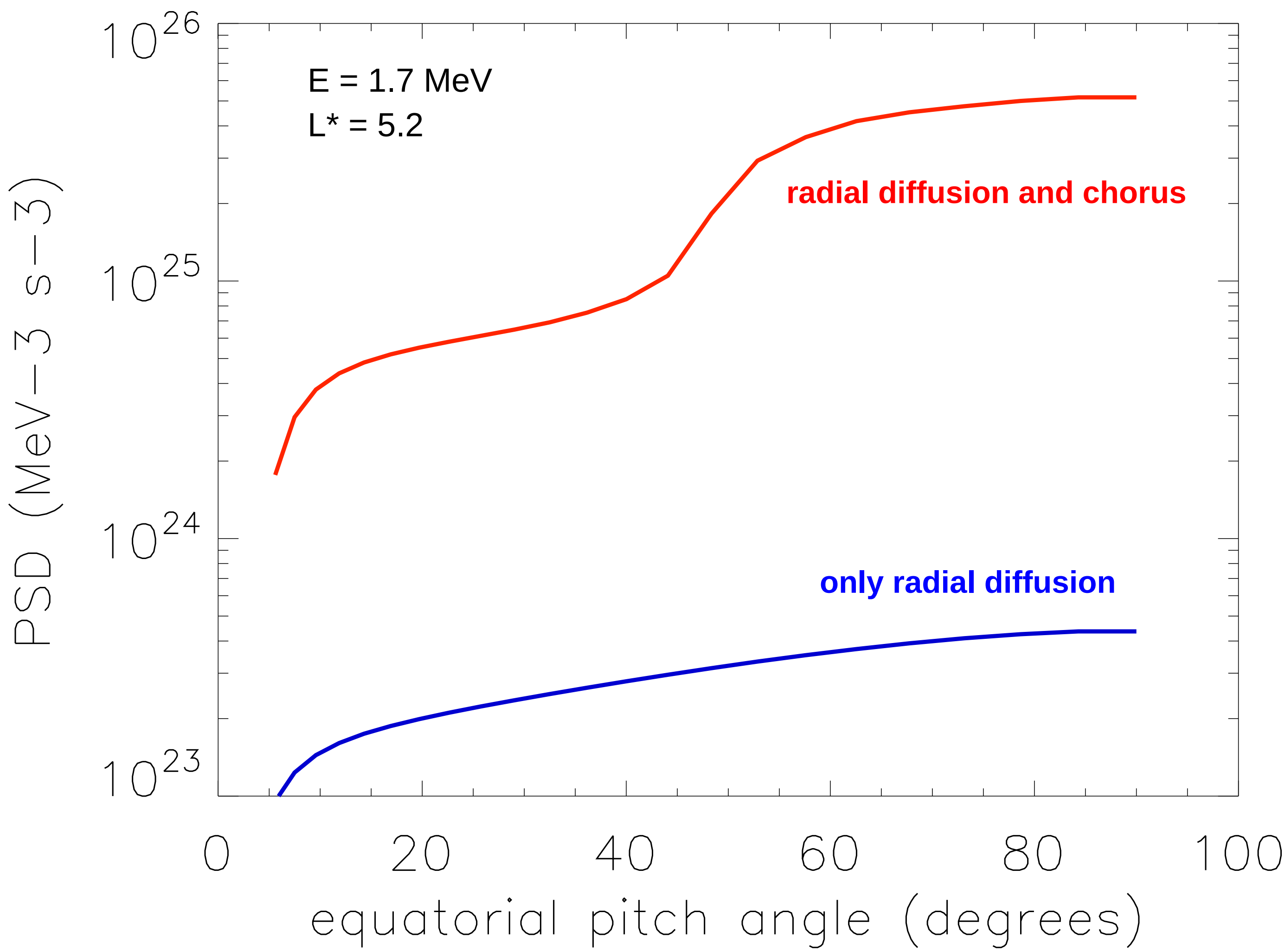

Figure 3. Steady state phase space density as a function of equatoral pitch angle for 1.7 MeV electrons at L* = 5.2 and for Kp = 1.3, for two simulations: (a) including chorus wave interactions (red line) and (b) including only radial diffusion (blue line).

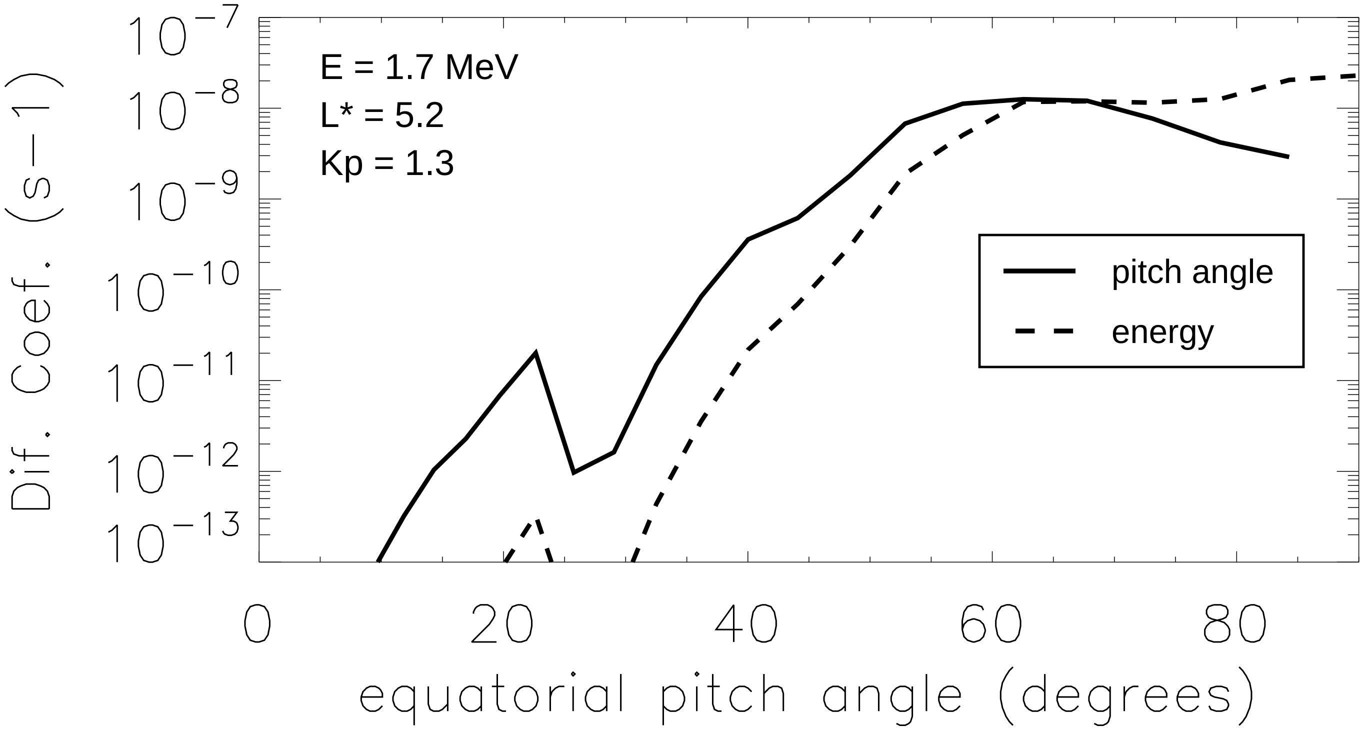

Figure 4. Energy and pitch angle diffusion coefficients (in s−1) as a function of equatorial pitch angle, for L* = 5.2, E = 1.7 MeV and Kp = 1.3.

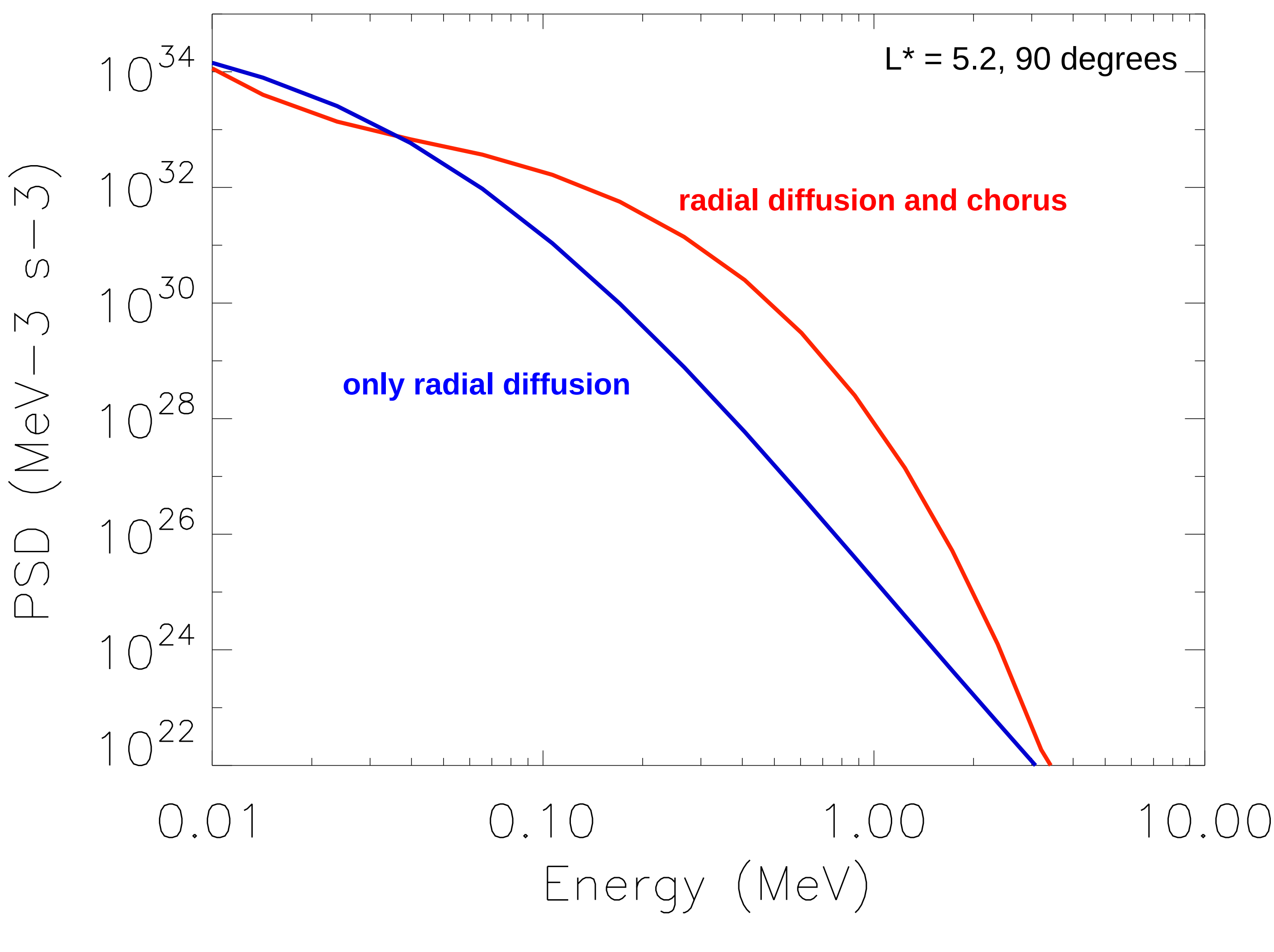

Figure 5. Steady state phase space density (in MeV−3 s−3) as a function of energy for equatorial particles at L* = 5.2 and for Kp = 1.3, for two simulations: including chorus wave interactions (red line) and including only radial diffusion (blue line).

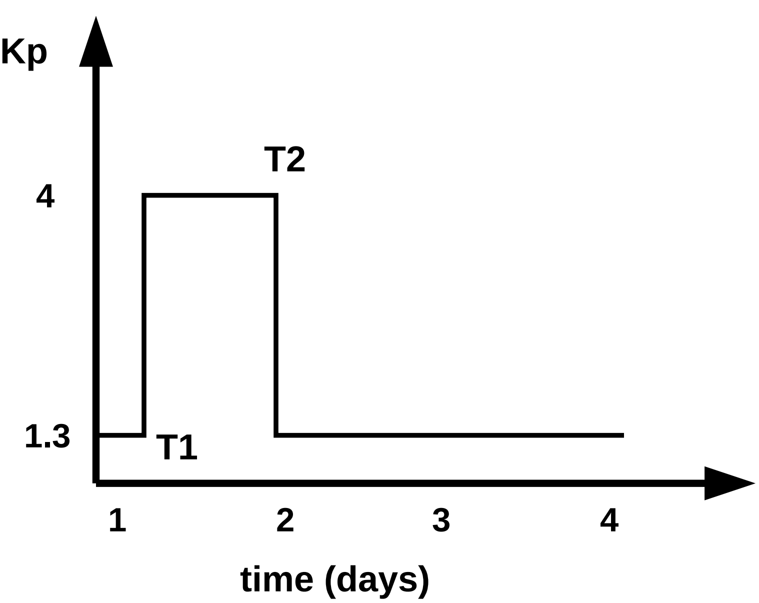

Figure 6. Kp profile for the dynamic test case simulation.

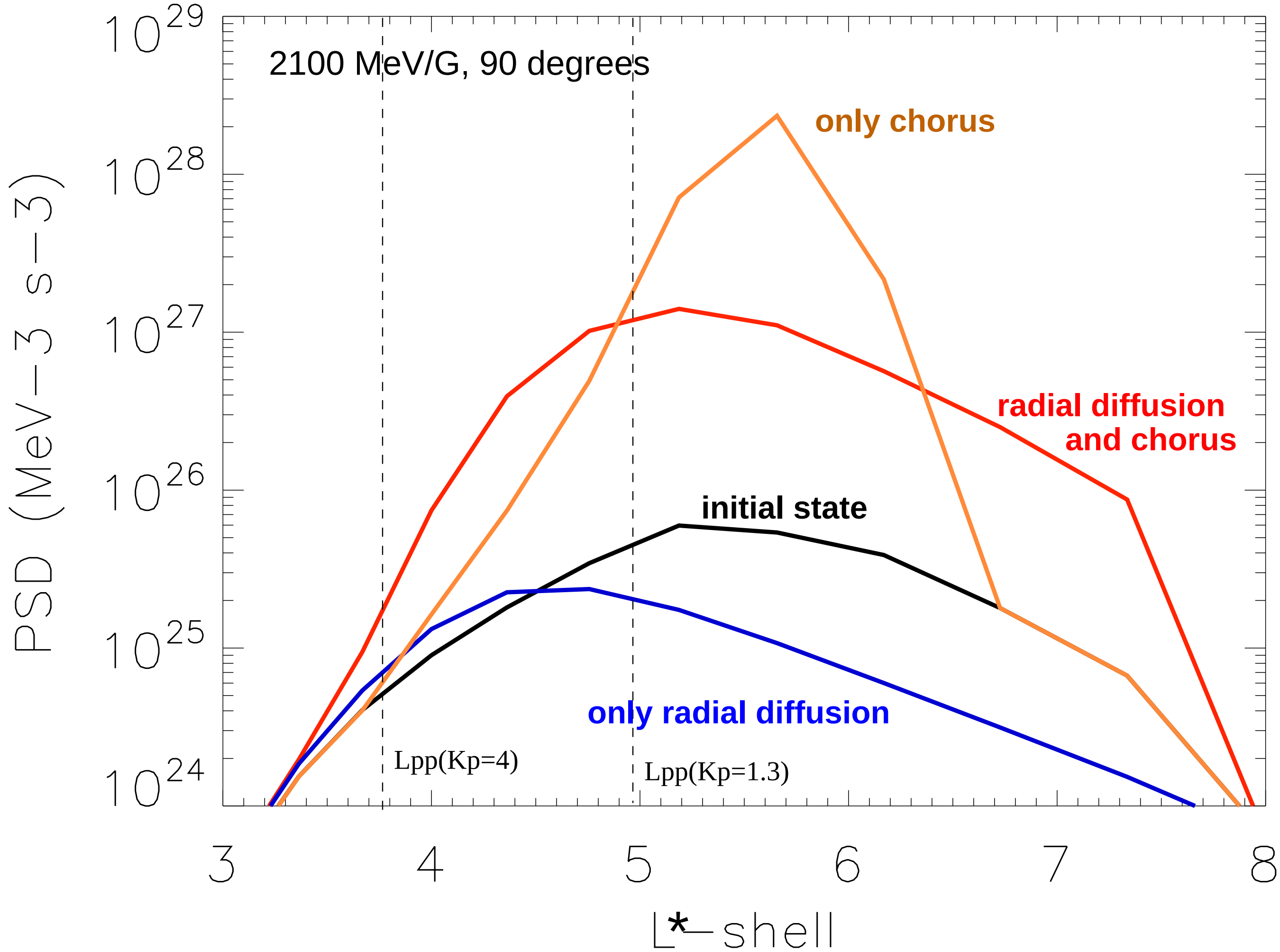

Figure 7. Phase Space densities (in MeV−3 s−3) for 2100 MeV/G equatorial particles as a function of L* from the three simulations at time T2: including only chorus wave interactions (orange line), including only radial diffusion (blue line) and including both processes (red line), starting from the same initial state (black line. Dashed lines show the position of the plasmapause for Kp = 1.3 and Kp = 4.

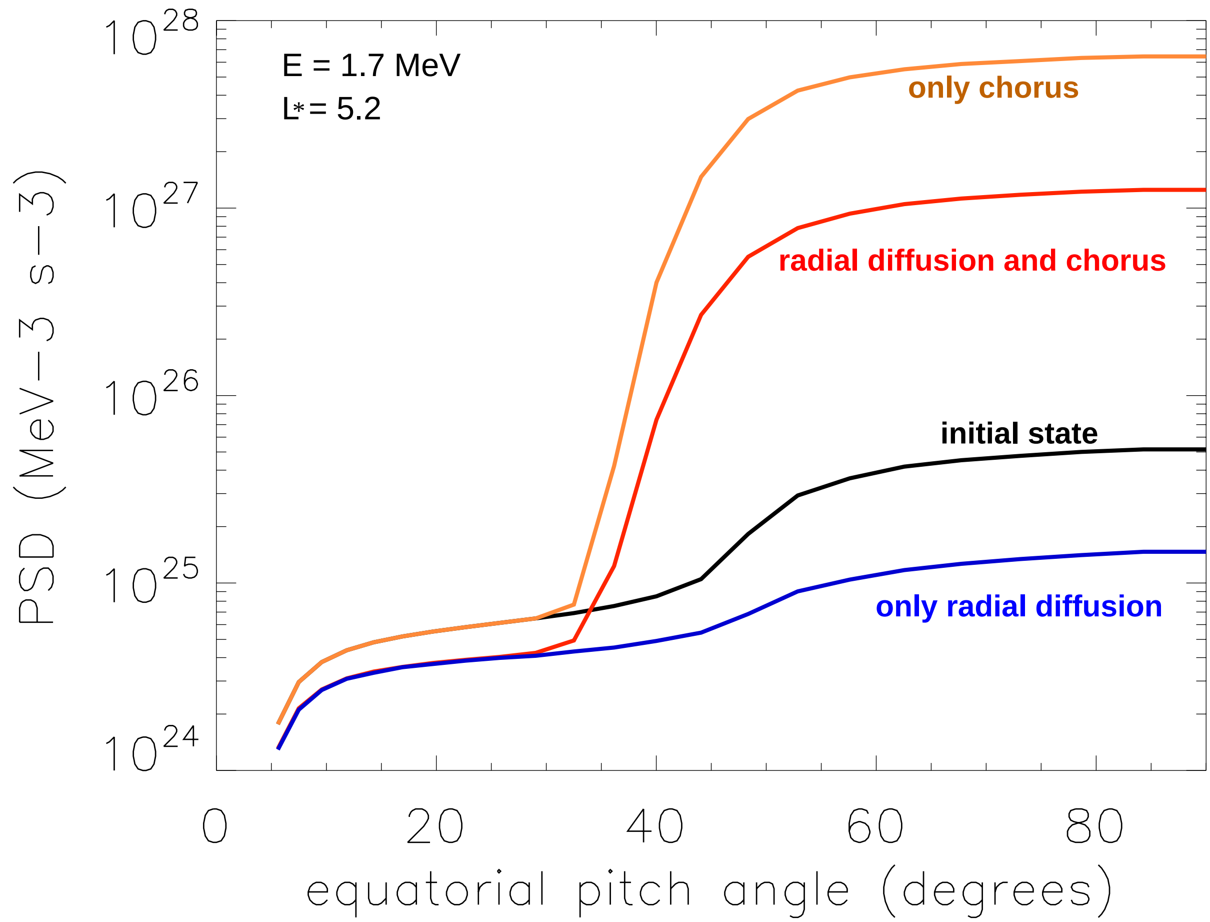

Figure 8. Phase space densities for 1.7 MeV electrons at L* = 5.2 as a function of equatorial pitch angle from the three simulations at time T2: including only chorus wave interactions (orange line), including only radial diffusion (blue line) and including both processes (red line),starting from the same initial state (black line).

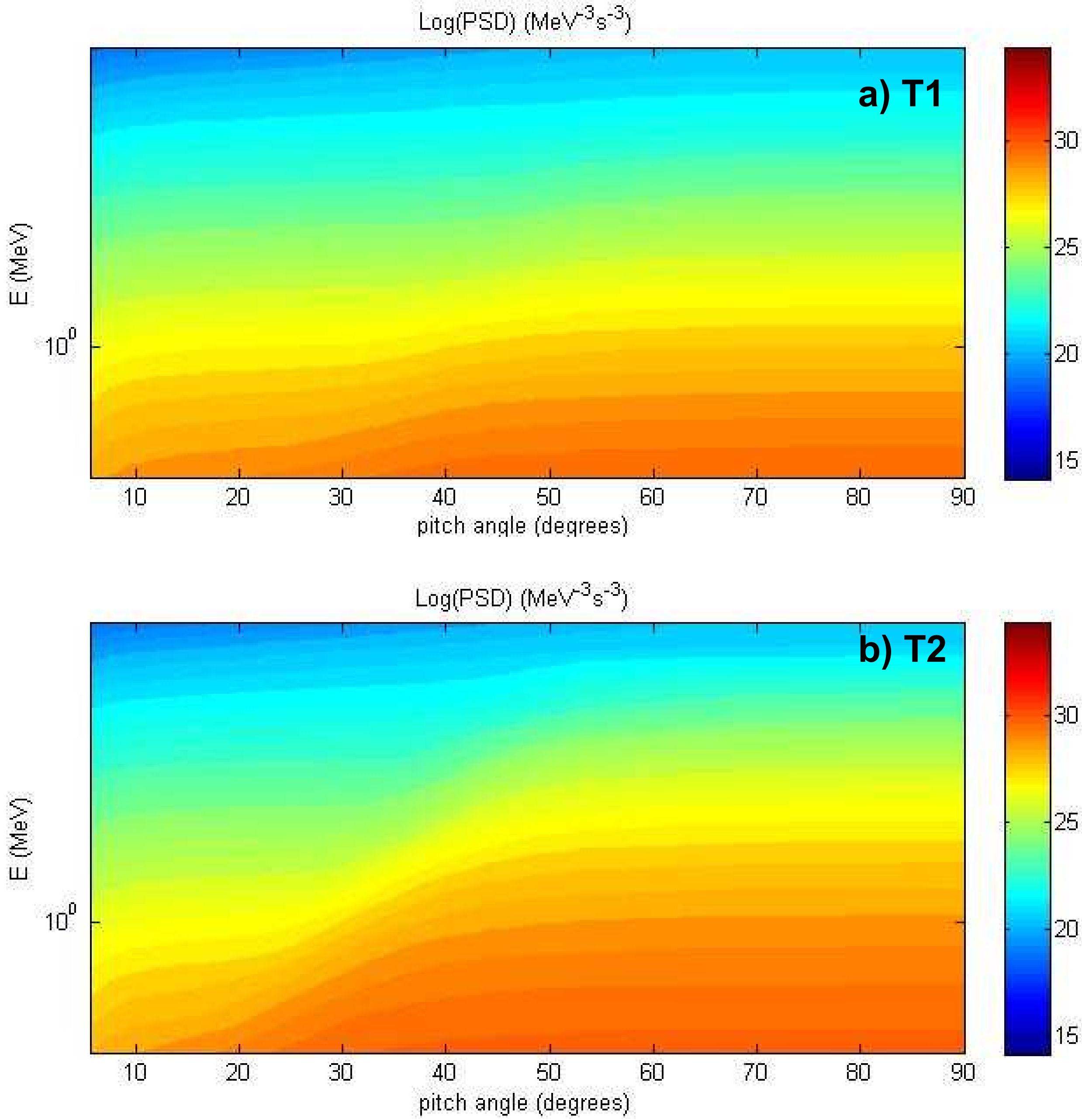

Figure 9. 2D plots of phase space densities at $L^* = 5.2$ as a function of energy (shown from 0.5 to 5 MeV on a log scale) and equatorial pitch angle at a) time T1 and b) time T2.

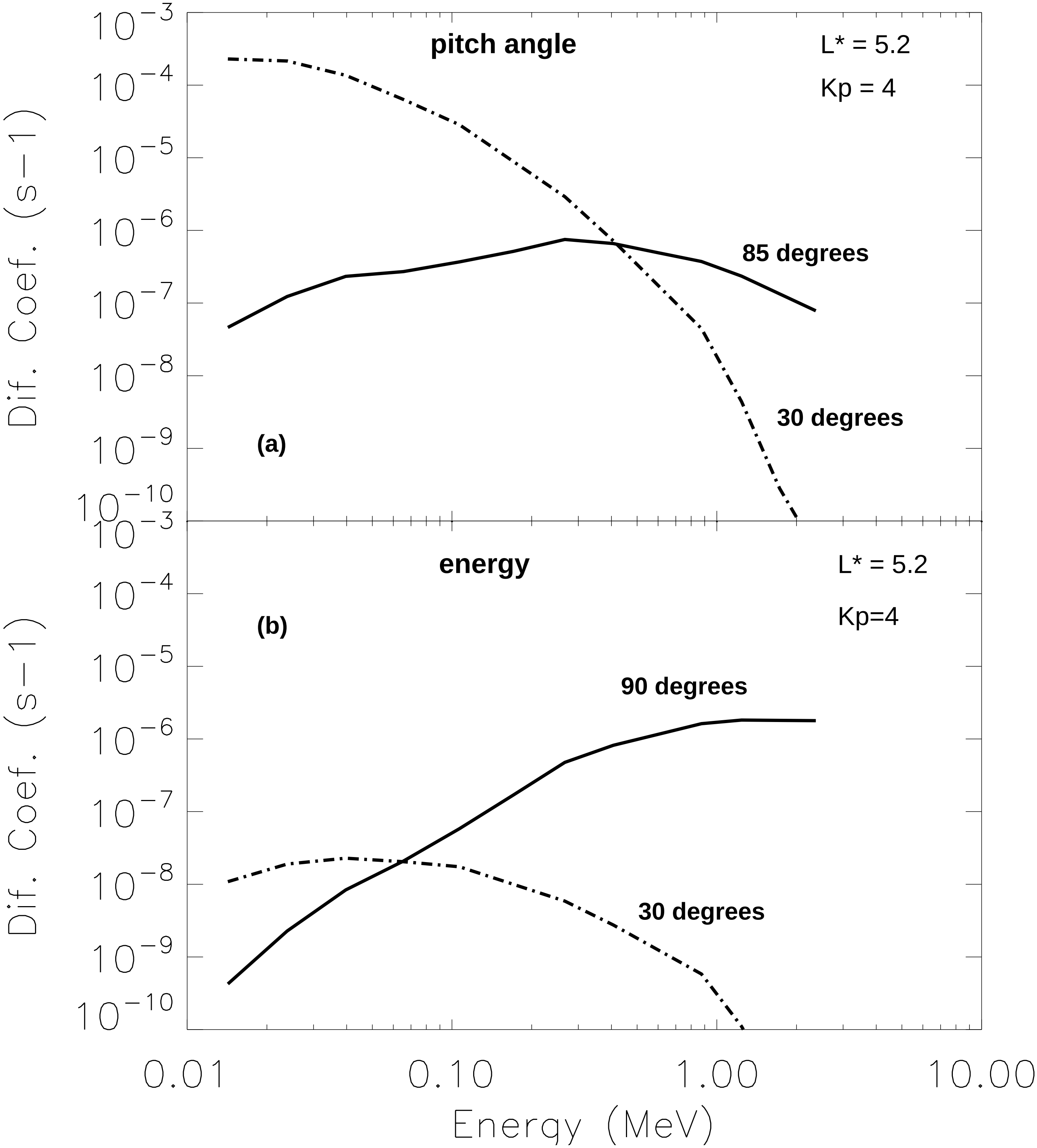

Figure 10. Diffusion coefficients as a function of energy for Kp = 4 and L* = 5.2: (a) pitch angle diffusion coefficients at 90 degrees (solid line) and 30 degrees (dash dot line) and (b) energy diffusion coefficients at 90 degrees (solid line) and 30 degrees (dash dot line).

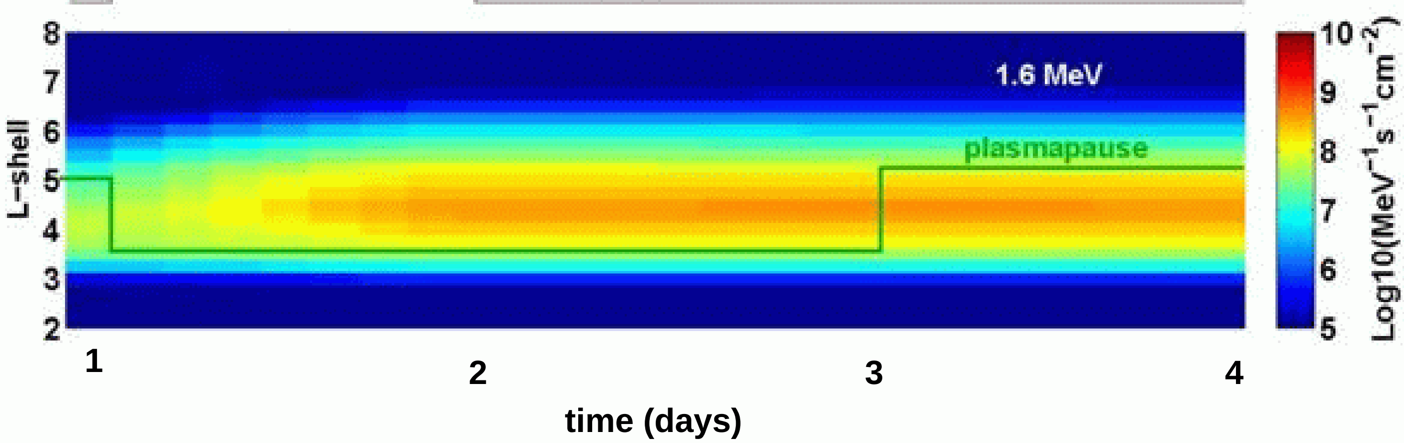

Figure 11. Omnidirectional equatorial flux variation during the test−case simulation for 1.6 MeV electrons. The plasmapause position is marked with a green line.

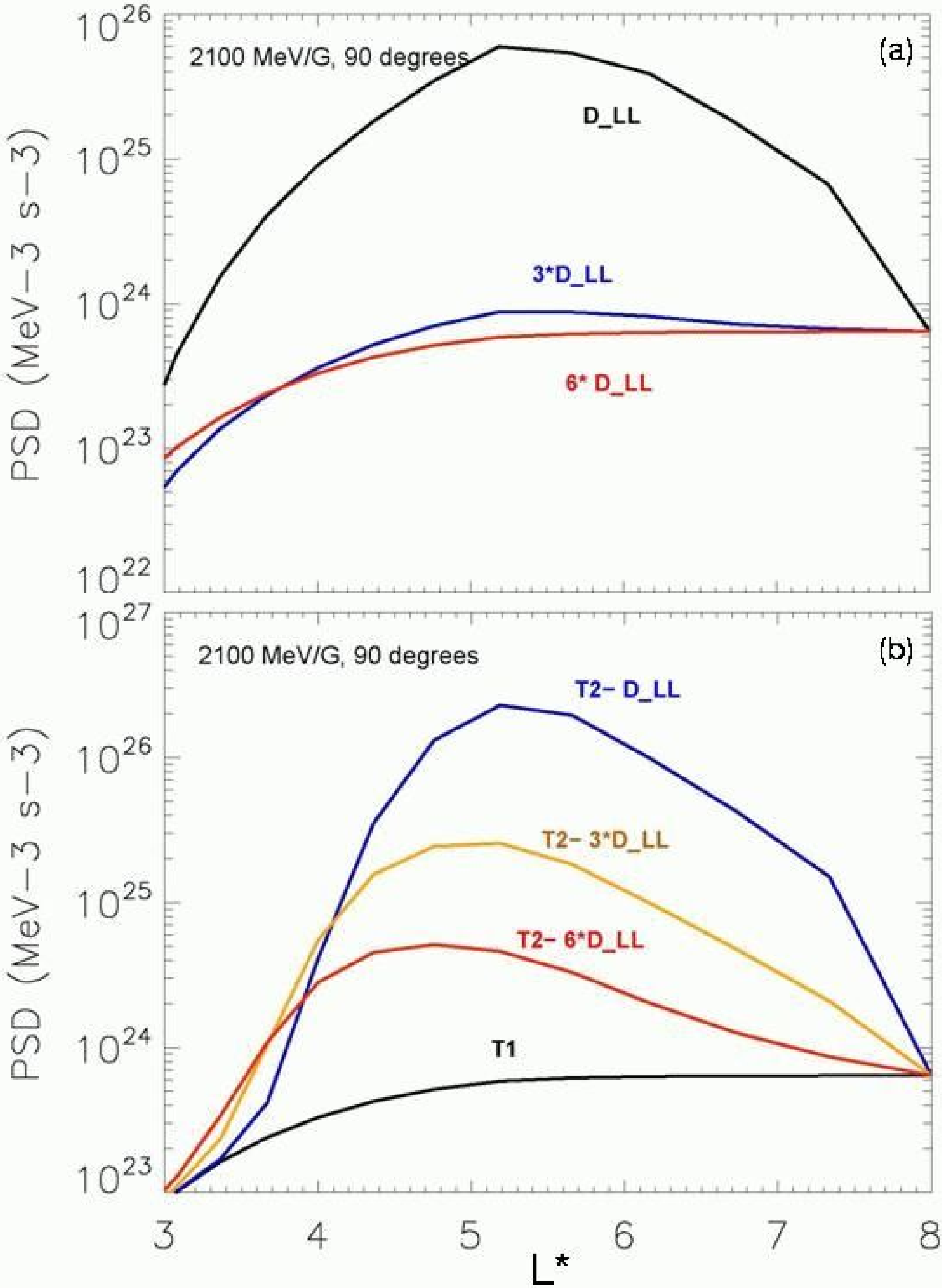

Figure 12. Phase space densities (in MeV−3s−3) for 2100 MeV/G equatorial particles as a function of L* for (a) the three steady state simulations and (b) at time T2 for the three dynamic simulations starting from the same initial state at T1.

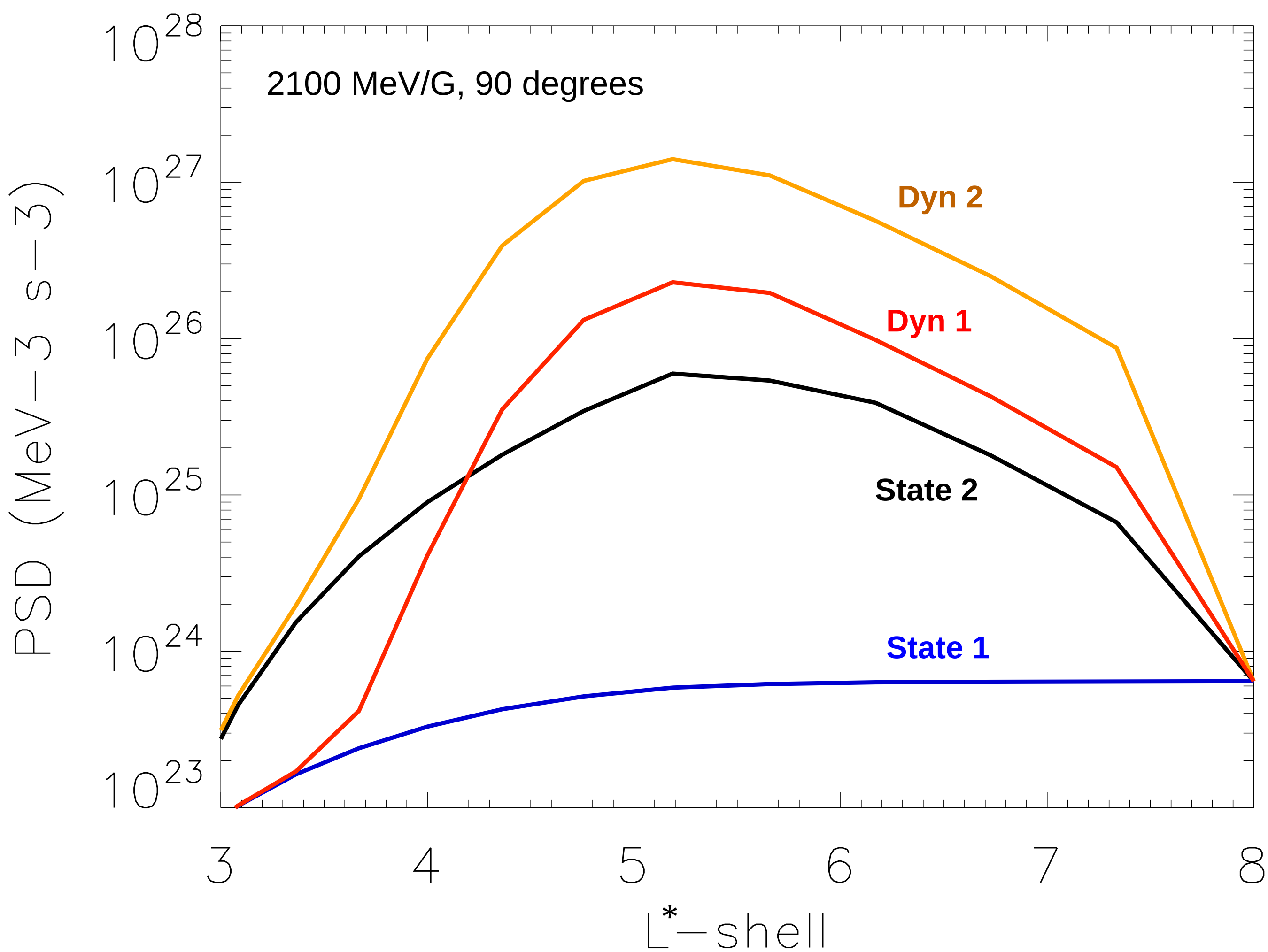

Figure 13. Phase space densities for 2100 meV/G equatorial particles as a function of L* at times T1 and T2 from two dynamic simulations: one starting from State 1 and one starting from State 2.

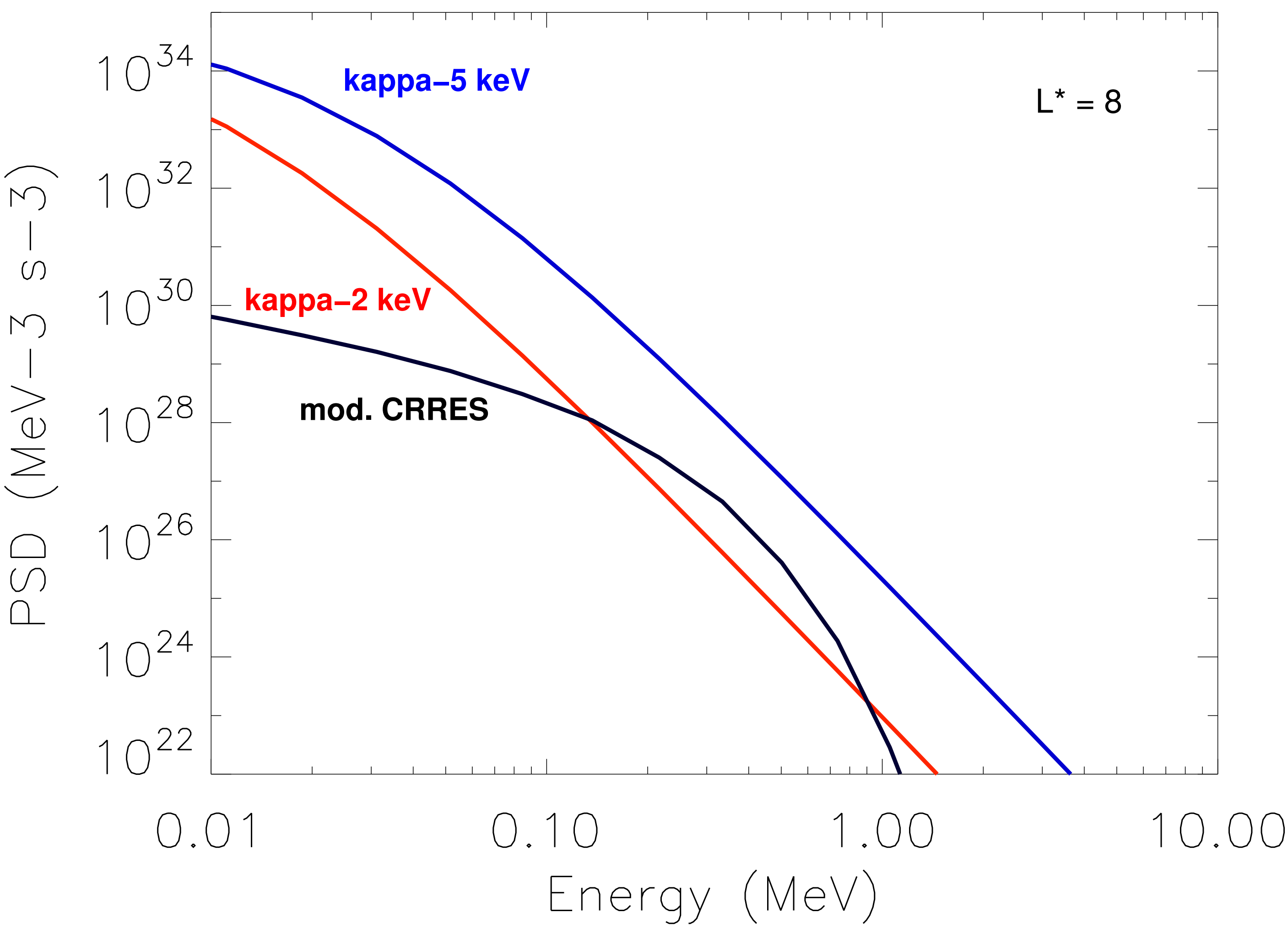

Figure 14. Spectrum of the three distributions used as a source at the outer boundary (L* = 8): the kappa distribution with Eo = 2 keV (red), the kappa distribution with Eo = 5 keV (blue) and the distribution taken from CRRES (black).

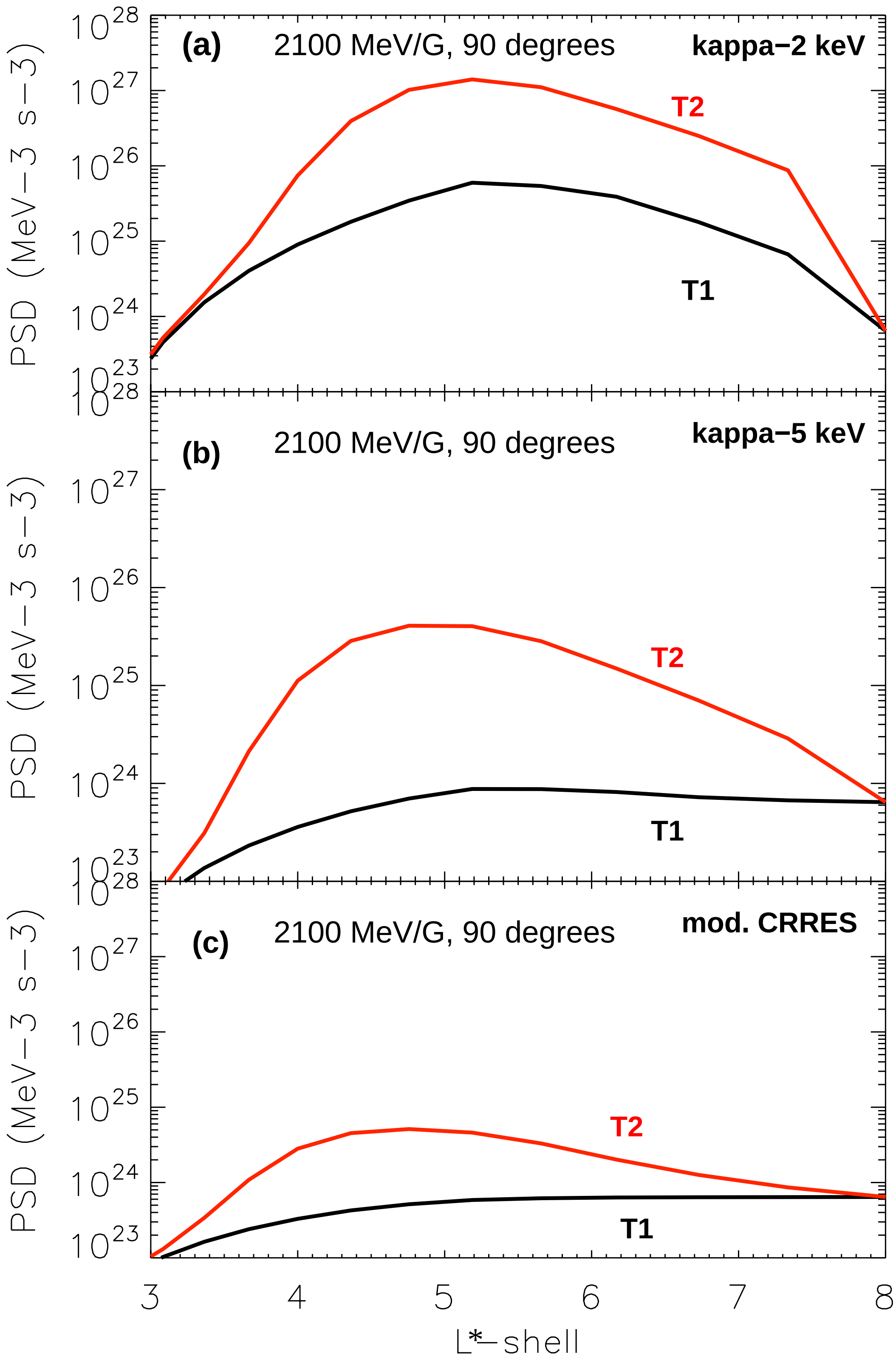

Figure 15. Phase space densities for 2100 MeV/G equatorial particles as a function of L* at times T1 and T2 using the three boundary conditions (a) a kappa distribution with Eo = 2 keV, (b) the kappa distribution with Eo = 5 keV and (c) the distribution taken from CRRES.